An ancestral interaction module promotes oligomerisation in divergent mitochondrial ATP synthases

Ondřej Gahura[1,†], Alexander Mühleip[3,4,†], Carolina Hierro-Yap[1,2], Brian Panicucci[1], Minal Jain[1,2], David Hollaus[2], Martina Slapničková[1], A. Amunts[3,4,*], Alena Zíková[1,2,*]

[1]Institute of Parasitology, Biology Centre CAS, Ceske Budejovice, Czech Republic

[2]Faculty of Science, University of South Bohemia, Ceske Budejovice, Czech Republic

[3]Science for Life Laboratory, Department of Biochemistry and Biophysics, Stockholm University, 17165 Solna, Sweden

[4]Department of Medical Biochemistry and Biophysics, Karolinska Institutet, 17177 Stockholm, Sweden

[*]Correspondence to: amunts@scilifelab.se; azikova@paru.cas.cz

[†]These authors contributed equally to this work.

Abstract

Mitochondrial ATP synthase forms stable dimers arranged into oligomeric assemblies that generate the inner-membrane curvature essential for efficient energy conversion. Here, we report cryo-EM structures of the intact ATP synthase dimer from trypanosomes in 10 different rotational states. The model consists of 25 subunits, including 11 lineage-specific, as well as 36 lipids. The rotary mechanism is influenced by the divergent peripheral stalk, conferring a greater conformational flexibility. Proton transfer in the lumenal half-channel occurs via a chain of five ordered water molecules. The dimerization interface is formed by subunit-*g* that is critical for interactions but not for the catalytic activity. Although overall dimer architecture varies among eukaryotes, we find that subunit-*g* and -*e* form a common ancestral oligomerisation motif, which is shared between the trypanosomal and mammalian lineages. Therefore, our data defines the subunit-*g/e* module as a structural component determining ATP synthase oligomeric assemblies.

Main

Mitochondrial ATP synthase consists of the soluble F_1 and membrane-bound F_o subcomplexes, and occurs in dimers that assemble into oligomers to induce the formation of cristae folds. The cristae folds are the sites for oxidative phosphorylation and energy conversion in eukaryotic cells. Dissociation of ATP synthase dimers into monomers results in the loss of native cristae architecture and impairs mitochondrial function[1,2]. While the cristae morphology varies substantially between organisms from different lineages, ranging from flat lamellar in opisthokonts to coiled tubular in ciliates and discoidal in euglenozoans[3], the ATP synthase dimers represent a universal occurrence to maintain the membrane shape[4].

ATP synthase dimers of variable size and architecture, classified into types I to IV have recently been resolved by high-resolution cryo-EM studies. In the structure of the type-I ATP synthase dimer from mammals, the monomers are only weakly associated[5,6], and in yeast insertions in the membrane subunits form tighter contacts[7]. The structure of the type-II ATP synthase dimer from the alga *Polytomella* showed that the dimer interface is formed by phylum-specific components[8]. The type-III ATP synthase dimer from a ciliate *Tetrahymena* is characterized by parallel rotary axes, and a substoichiometric subunit, as well as multiple lipids were identified at the dimer interface, while additional protein components that tie the monomers together are distributed between the matrix, transmembrane, and lumenal regions[9]. The structure of the type-IV ATP synthase with native lipids from *Euglena* also showed that specific protein-lipid interactions contribute to the dimerization, and that the central and peripheral stalks interact with each other directly[10]. Finally, a unique apicomplexan ATP synthase dimerises via 11 parasite-specific components that contribute ~7000 Å² buried surface area[11], and unlike all other ATP synthases, that assemble into rows, it associates in higher oligomeric states of pentagonal pyramids in the curved apical membrane regions. Together, the available structural data suggest a diversity of oligomerisation, and it remains unknown whether common elements mediating these interactions exist or the dimerization of ATP synthase occurred independently and multiple times in evolution[4].

The ATP synthase of *Trypanosoma brucei*, a representative of kinetoplastids an established medically important model organism causing the sleeping sickness, is highly divergent, exemplified by the pyramid-shaped F_1 head containing a phylum specific subunit[12,13]. The dimers are sensitive to the lack of cardiolipin[14] and form short left-handed helical segments that extend across the membrane ridge of the discoidal cristae[15]. Uniquely among aerobic eukaryotes, the mammalian life cycle stage of *T. brucei* utilizes the ATP synthase as a proton pump maintaining the mitochondrial membrane potential at the expense of ATP[16,17], whereas the insect stage of the parasite employs the forward ATP-producing mode of the enzyme[18,19].

Given the conservation of the core subunits, the different nature of oligomerisation and the ability to test structural hypotheses biochemically, we reasoned that investigation of the *T. brucei* ATP synthase structure and function would provide the missing evolutionary link to understand how the monomers interact to form physiological dimers. Here, we address this question by combining structural, functional and evolutionary analysis of the *T. brucei* ATP synthase dimer.

2

Results

Cryo-EM structure of the *T. brucei* ATP synthase

We purified ATP synthase dimers from cultured *T. brucei* procyclic trypomastigotes by affinity chromatography with a recombinant natural protein inhibitor TbIF$_1$[20], and subjected to cryo-EM analysis (Supplementary Fig. 1 and 2). Using masked refinements, maps were obtained for the membrane region, the rotor, and the peripheral stalk. To further describe the conformational space of the *T. brucei* ATP synthase, we resolved 10 distinct rotary substates, which were refined to 3.5-4.3 Å resolution. Finally, particles with both monomers in rotational state 1 were selected, and the consensus structure of the dimer was refined to 3.2 Å resolution (Supplementary Table 1, Supplementary Fig. 2).

Unlike the wide-angle architecture of dimers found in animals and fungi, the *T. brucei* ATP synthase displays an angle of 60° between the two F_1/*c*-ring subcomplexes. The model of the *T. brucei* ATP synthase includes all 25 different subunits, 11 of which are lineage-specific (Fig. 1a, Supplementary Video 1, Supplementary Fig. 3). We named the subunits according to the previously proposed nomenclature[21-23] (Supplementary Table 2). In addition, we identified and modeled 36 bound phospholipids, including 24 cardiolipins (Supplementary Fig. 4). Both detergents used during purification, n-dodecyl β-D-maltoside (β-DDM) and glyco-diosgenin (GDN) are also resolved in the periphery of the membrane region (Supplementary Fig. 5).

In the catalytic region, F_1 is augmented by three copies of subunit p18, each bound to subunit-α[12,13]. Our structure shows that p18 is involved in the unusual attachment of F_1 to the peripheral stalk. The membrane region includes seven conserved F_o subunits (*d*, *f*, 8, *i/j*, *k*, *e*, and *g*) arranged around the central proton translocator subunit-*a*. We identified those subunits based on the structural similarity and matching topology to their yeast counterparts (Fig 2). Surprisingly, the long helix-2 of subunit-*b* (*b*H2), which constitutes the central part of the peripheral stalk in other organisms and associates with subunit-*a* in the membrane, is absent in *T. brucei.* By contrast, *b*H1 from the yeast structure superposes well with the single transmembrane helix of ATPTB14, which anchors the newly identified subunit-*e* and -*g* to the F_o (Fig 2a). Therefore, ATPTB14 may represent a highly reduced homolog of subunit-*b*.

The membrane region contains a peripheral subcomplex, formed primarily by the phylum-specific ATPTB1,6,12 and ATPEG3 (Fig. 1b). It is separated from the conserved core by a membrane-intrinsic cavity, in which nine bound cardiolipins are resolved (Fig. 1c), and the C-terminus of ATPTB12 interacts with the lumenal β-barrel of the c_{10}-ring. In the cavity of the decameric *c*-ring near the matrix side, 10 Arg66$_c$ residues coordinate a ligand density, which is consistent with a pyrimidine ribonucleoside triphosphate (Fig. 1d). We assign this density as uridine-triphosphate (UTP), due to its large requirement in the mitochondrial RNA metabolism of African trypanosomes being a substrate for post-transcriptional RNA editing[24], and addition of poly-uridine tails to gRNAs and rRNAs[25,26], as well as due to low abundance of cytidine triphosphate (CTP)[27]. The nucleotide base is inserted between two Arg82$_c$ residues, whereas the triphosphate region is coordinated by another five Arg82$_c$ residues, with Tyr79$_\delta$ and Asn76$_\delta$ providing asymmetric coordination contacts. The presence of a nucleotide inside the *c*-ring is surprising, given the recent reports of phospholipids inside the *c*-rings in mammals[5,6] and ciliates[9], indicating that a range of different ligands can provide structural scaffolding.
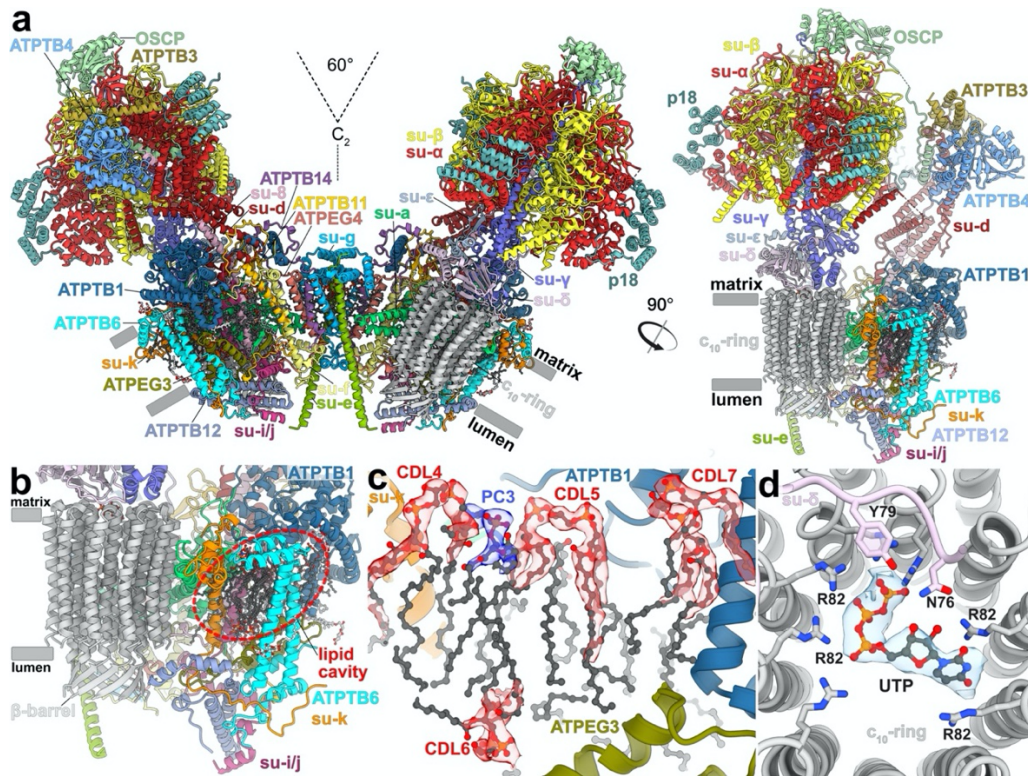
Fig. 1: The *T. brucei* ATP synthase structure with lipids and ligands.

a, Front and side views of the composite model with both monomers in rotational state 1. The two F_1/c_{10}-ring complexes, each augmented by three copies of the phylum-specific p18 subunit, are tied together at a 60°-angle. The membrane-bound F_o region displays a unique architecture and is composed of both conserved and phylum-specific subunits. **b**, Side view of the F_o region showing the lumenal interaction of the ten-stranded β-barrel of the *c*-ring (grey) with ATPTB12 (pale blue). The lipid-filled peripheral F_o cavity is indicated. **c**, Close-up view of the bound lipids within the peripheral F_o cavity with cryo-EM density shown. **d**, Top view into the decameric *c*-ring with a bound pyrimidine ribonucleoside triphosphate, assigned as UTP. Map density shown in transparent blue, interacting residues shown.


Fig. 2: Identification of conserved F_o subunits.

a, Top view of the membrane region with *T. brucei* subunits (colored) overlayed with *S. cerevisiae* structure (gray transparent). Close structural superposition and matching topology allowed the assignment of conserved subunits based on matching topology and location. **b**, Superposition of subunits-*e* and -*g* with their *S. cerevisiae* counterparts (PDB 6B2Z) confirms their identity.

4

Peripheral stalk flexibility and distinct rotational states

The trypanosomal peripheral stalk displays a markedly different architecture compared to its yeast and mammalian counterparts. In the opisthokont complexes, the peripheral stalk is organized around the long bH2, which extends from the membrane ~15 nm into the matrix and attaches to OSCP at the top of F_1[5,7]. By contrast, *T. brucei* lacks the canonical bH2 and instead, helices 5-7 of divergent subunit-d and the C-terminal helix of extended subunit-8 bind to a C-terminal extension of OSCP at the apical part of the peripheral stalk (Fig. 3a). The interaction between OSCP and subunit-d and -8 is stabilized by soluble ATPTB3 and ATPTB4. The peripheral stalk is rooted to the membrane subcomplex by a transmembrane helix of subunit-8, wrapped on the matrix side by helices 8-11 of subunit-d. Apart from the canonical contacts at the top of F_1, the peripheral stalk is attached to the F_1 via a euglenozoa-specific C-terminal extension of OSCP, which contains a disordered linker and a terminal helix hairpin extending between the F_1-bound p18 and subunits -d and -8 of the peripheral stalk (Fig. 3a, Supplementary Videos 2,3). Another interaction of F_1 with the peripheral stalk occurs between the stacked C-terminal helices of subunit-β and -d (Fig. 3b), the former of which structurally belongs to F_1 and is connected to the peripheral stalk via a flexible linker.

To assess whether the unusual peripheral stalk architecture influences the rotary mechanism, we analysed 10 classes representing different rotational states. The three main states (1-3) result from ~120° rotation of the central stalk subunit-γ, and we identified five (1a-1e), four (2a-2d) and one (3) classes of the respective main states. The rotor positions of the rotational states 1a, 2a and 3 are related by steps of 117°, 136° and 107°, respectively. Throughout all the identified substeps of the rotational state 1 (classes 1a to 1e) the rotor turns by ~33°, which corresponds approximately to the advancement by one subunit-c of the c_{10}-ring. While rotating along with the rotor, the F_1 headpiece lags behind, advancing by only ~13°. During the following transition from 1e to 2a, the rotor advances by ~84°, whereas the F_1 headpiece rotates ~22° in the opposite direction (Fig. 3c,d). This generates a counter-directional torque between the two motors, which is consistent with a power-stroke mechanism. Albeit with small differences in step size, this mechanism is consistent with a previous observation in the *Polytomella* ATP synthase[8]. However, due to its large, rigid peripheral stalk, the *Polytomella* ATP synthase mainly displays rotational substeps, whereas the *Trypanosoma* F_1 also displays a tilting motion of ~8° revealed by rotary states 1 and 2 (Fig. 3e, Supplementary Video 2). The previously reported hinge motion between the N- and C-terminal domains of OSCP[8] is not found in our structure, instead, the conformational changes of the F_1/c_{10}-ring subcomplex are accommodated by a 5° bending of the apical part of the peripheral stalk. (Fig. 3e, Supplementary Videos 2,3). Together, the structural data indicate that the divergent peripheral stalk attachment confers greater conformational flexibility to the *T. brucei* ATP synthase.
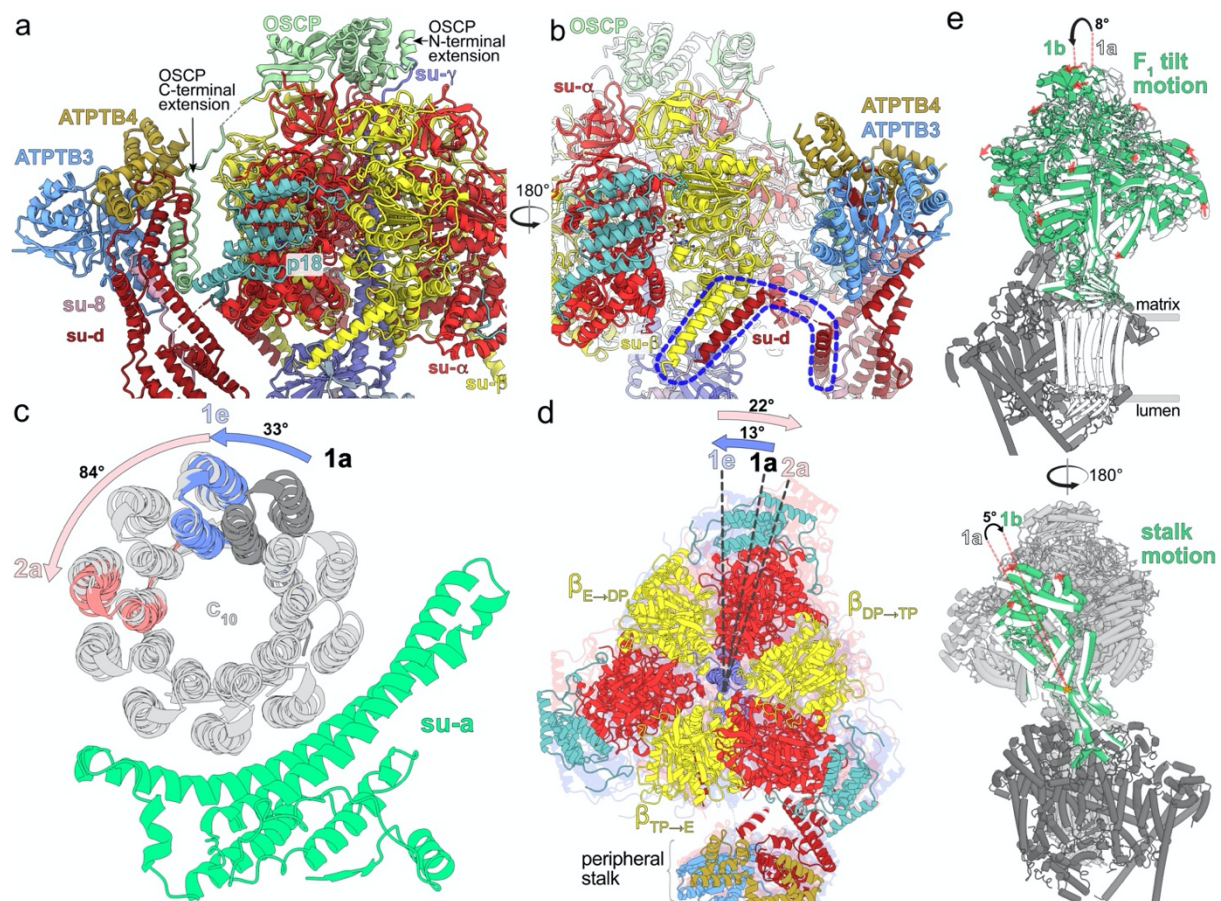
Fig. 3: A divergent peripheral stalk allows high flexibility during rotary catalysis. a, N-terminal OSCP extension provides a permanent central stalk attachment, while the C-terminal extension provides a phylum-specific attachment to the divergent peripheral stalk. **b**, The C-terminal helices of subunits -β and -d provide a permanent F_1 attachment. **c**, Substeps of the c-ring during transition from rotational state 1 to 2. **d**, F_1 motion accommodating steps shown in (c). After advancing along with the rotor to state 1e, the F_1 rotates in the opposite direction when transitioning to state 2a. **e**, Tilting motion of F_1 and accommodating bending of the peripheral stalk.

Lumenal proton half-channel is insulated by a lipid and contains ordered water molecules

The mechanism of proton translocation involves sequential protonation of E102 of subunits-c, rotation of the c_{10}-ring with neutralized E102c exposed to the phospholipid bilayer, and release of protons on the other side of the membrane. The sites of proton binding and release are separated by the conserved R146 contributed by the horizontal helix H5 of subunit-a and are accessible from the cristae lumen and mitochondrial matrix by aqueous half channels (Fig. 4a). Together, R146 and the adjacent N209 coordinate a pair of water molecules in between helices H5 and H6 (Fig. 4b). A similar coordination has been observed in the *Polytomella* ATP synthase[8]. The coordination of water likely restricts the R146 to rotamers that extend towards the c-ring, with which it is thought to interact.

In our structure, the lumenal half-channel is filled with a network of resolved water densities, ending in a chain of five ordered water molecules (W1-W5; Fig. 4c,d,e). The presence of

6

194 ordered water molecules in the aqueous channel is consistent with a Grotthuss-type mechanism
195 for proton transfer, which would not require long-distance diffusion of water molecules[5].
196 However, because some distances between the observed water molecules are too large for
197 direct hydrogen bonding, proton transfer may involve both coordinated and disordered water
198 molecules. The distance of 7 Å between the last resolved water (W1) and D202$_a$, the conserved
199 residue that is thought to transfer protons to the *c*-ring, is too long for direct proton transfer.
200 Instead, it may occur via the adjacent H155$_a$. Therefore, our structure resolves individual
201 elements participating in proton transport (Fig. 4d,e).

202 The lumenal proton half-channel in the mammalian[5,6] and apicomplexan[11] ATP synthase is
203 lined by the transmembrane part of *b*H2, which is absent in *T. brucei*. Instead, the position of
204 *b*H2 is occupied by a fully ordered phosphatidylcholine in our structure (PC1; Fig. 4a,c).
205 Therefore, a bound lipid replaces a proteinaceous element in the proton path.
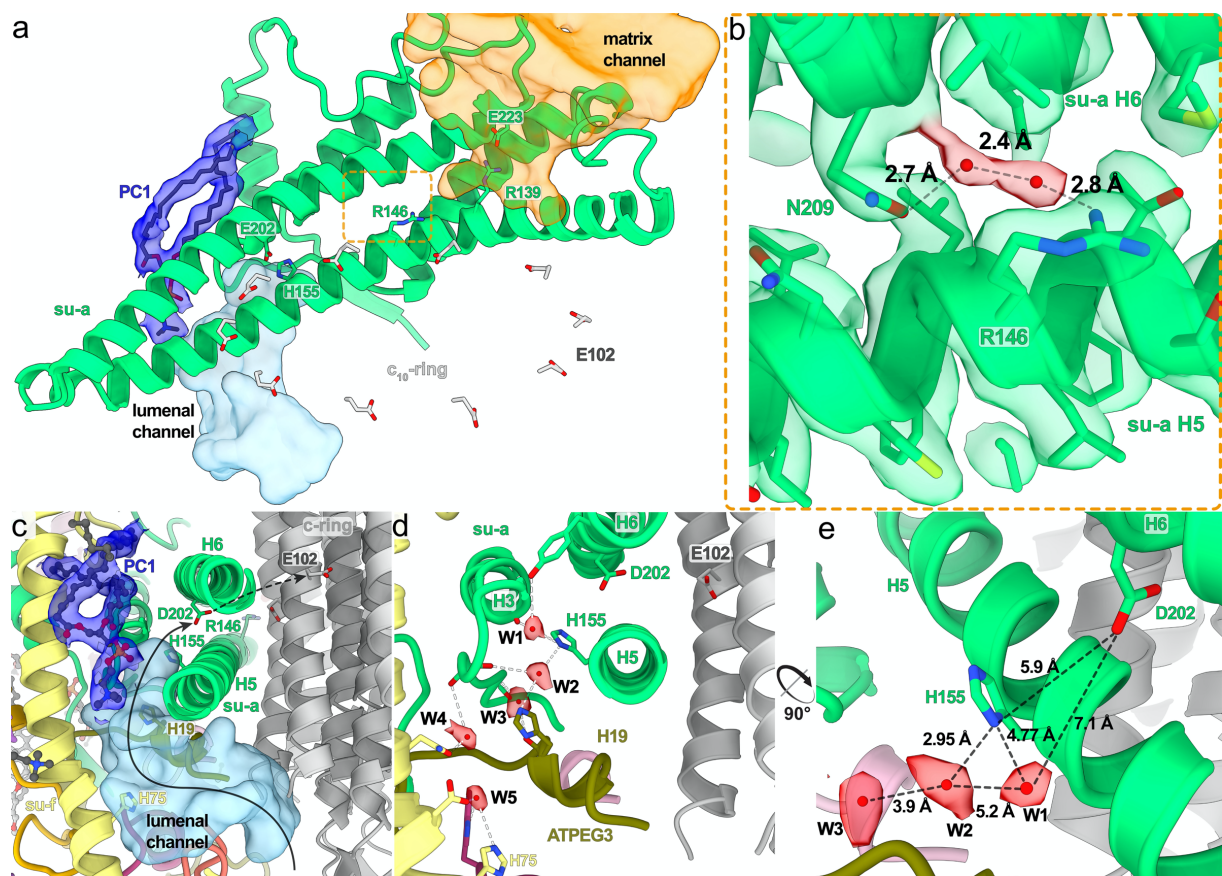
Fig. 4: The lumenal half-channel contains ordered water molecules and is confined by an F$_o$-bound lipid. a, Subunit-*a* (green) with the matrix (orange) and lumenal (light blue) channels, and an ordered phosphatidylcholine (PC1; blue). E102 of the c_{10}-ring shown in grey. **b**, Close-up view of the highly conserved R146$_a$ and N209$_a$, which coordinate two water molecules between helices H5-6$_a$. **c**, Sideview of the lumenal channel with proton pathway (light blue) and confining phosphatidylcholine (blue). **d**, Chain of ordered water molecules in the lumenal channel. Distances between the W1-W5 are 5.2, 3.9, 7.3 and 4.8 Å, respectively. **e**, The ordered waters extend to H155$_a$, which likely mediates the transfer of protons to D202$_a$.

7

Subunit-*g* facilitates assembly of different ATP synthase oligomers

Despite sharing a set of conserved F_o subunits, the *T. brucei* ATP synthase dimer displays a markedly different dimer architecture compared to all the previously determined structures. First, its interface of 3,600 Å^2 is smaller than that of the *E. gracilis* type-IV (10,000 Å^2) and the *T. thermophila* type-III ATP synthases (16,000 Å^2). Second, unlike mammalian and fungal ATP synthase, in which the peripheral stalks extend in the plane defined by the two rotary axes, in our structure the monomers are rotated such that the peripheral stalks are offset laterally on the opposite sides of the plane. Due to the rotated monomers, this architecture is associated with a specific dimerization interface, where two subunit-*g* copies interact homotypically on the C_2 symmetry axis (Fig. 5a, Supplemetary Video 1). Both copies of H1-2$_g$ extend horizontally along the matrix side of the membrane, clamping against each other (Fig. 5c,e). This facilitates formation of contacts between an associated transmembrane helix of subunit-*e* with the neighbouring monomer via subunit-*a'* in the membrane, and -*f'* in the lumen, thereby further contributing to the interface (Fig. 5b). Thus, the ATP synthase dimer is assembled via the subunit-*e/g* module. The C-terminal part of the subunit-*e* helix extends into the lumen, towards the ten-stranded β-barrel of the *c*-ring (Supplementary Fig. 6a). The terminal 23 residues are disordered with poorly resolved density connecting to the detergent plug of the *c*-ring β-barrel (Supplementary Fig. 6b). This resembles the lumenal C-terminus of subunit-*e* in the bovine structure[5], indicating a conserved interaction with the *c*-ring.

The *e/g* module is held together by four bound cardiolipins in the matrix leaflet, anchoring it to the remaining F_o region (Fig. 5c). The head groups of the lipids are coordinated by polar and charged residues with their acyl chains filling a central cavity in the membrane region at the dimer interface (Fig 5c, Supplementary Fig. 4f). Cardiolipin binding has previously been reported to be obligatory for dimerization in secondary transporters[28] and the depletion of cardiolipin synthase resulted in reduced levels of ATP synthase in the bloodstream trypanosomes[14].

Interestingly, for yeasts, early blue native gel electrophoresis[29] and subtomogram averaging studies[2] suggested subunit-*g* as potentially dimer-mediating, however the *e/g* modules are located laterally opposed on either side of the dimer long axis, in the periphery of the complex, ~8.5 nm apart from each other. Because the *e/g* module does not interact directly within the yeast ATP synthase dimer, they have been proposed to serve as membrane bending elements, whereas the major dimer contacts are formed by subunit-*a* and -*i/j*[7]. In mammals, the *e/g* module occupies the same position as in yeasts, forming the interaction between two diagonal monomers in a tetramer[5,6,30], as well as between parallel dimers[31]. The comparison with our structure shows that the overall organization of the intra-dimeric trypanosomal and inter-dimeric mammalian *e/g* module is structurally similar (Fig. 5d). Furthermore, kinetoplastid parasites and mammals share conserved GXXXG motifs in subunit-*e*[32] and -*g* (Supplementary Fig. 8), which allow close interaction of their transmembrane helices (Fig. 5e), providing further evidence for subunit homology. However, while the mammalian ATP synthase dimers are arranged perpendicularly to the long axis of their rows along the edge of cristae[33], the *T. brucei* dimers on the rims of discoidal cristae are inclined ~45º to the row axis[15]. Therefore, the *e/g* module occupies equivalent positions in the rows of both evolutionary distant groups (Fig. 5f and reference 31).

8
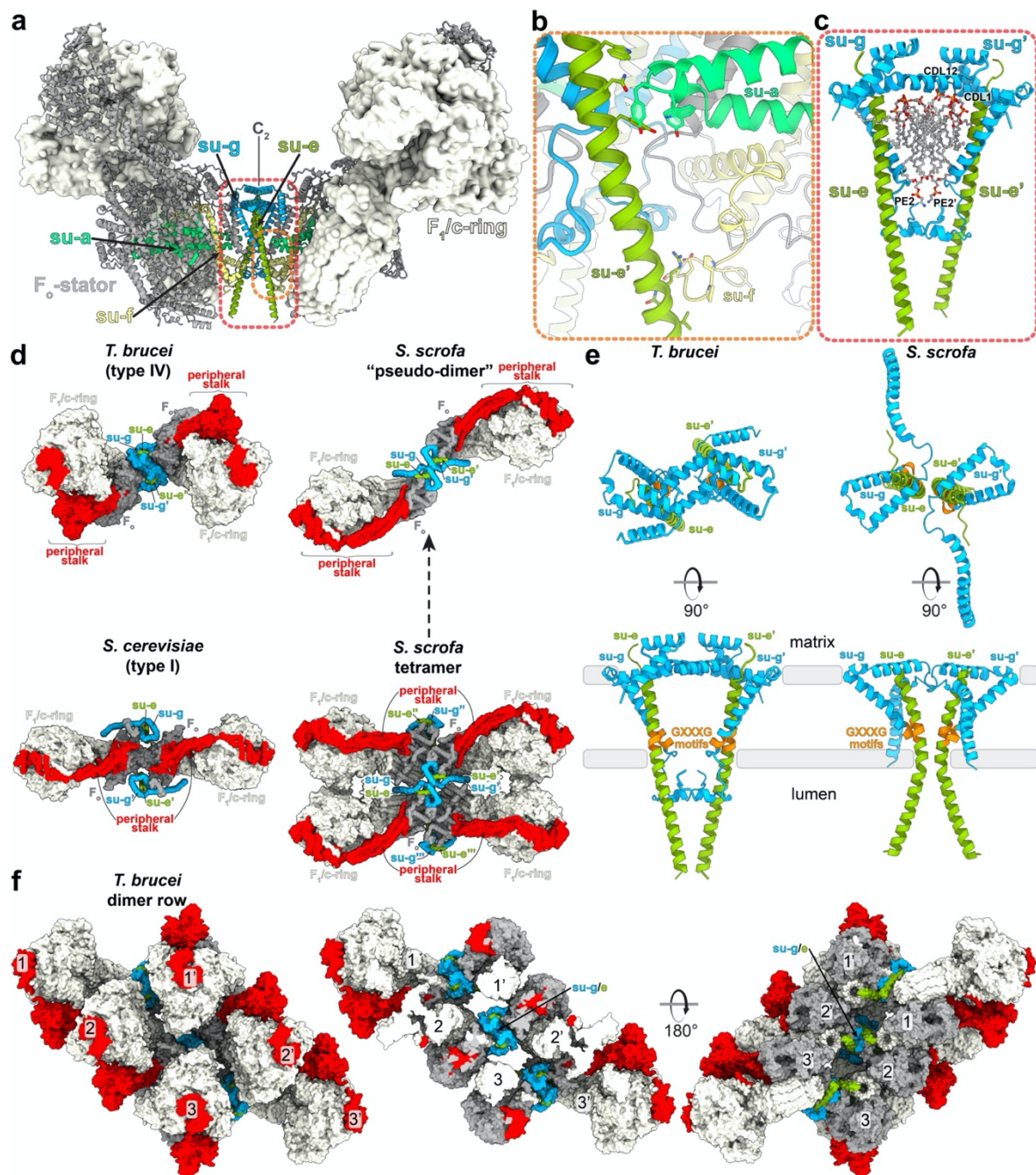
Fig. 5: The homotypic dimerization motif of subunit-*g* generates a conserved oligomerisation module. a, Side view with dimerising subunits colored. **b,c**, The dimer interface is constituted by (b) subunit-*e'* contacting subunit-*a* in the membrane and subunit-*f* in the lumen, (c) subunits *e* and *g* from both monomers forming a subcomplex with bound lipids. **d**, Subunit-*g* and -*e* form a dimerization motif in the trypanosomal (type-IV) ATP synthase dimer (this study), the same structural element forms the oligomerisation motif in the porcine ATP synthase tetramer. The structural similarity of the pseudo-dimer in the porcine structure with the trypanosomal dimer suggests that that type I and IV ATP synthase dimers have evolved through divergence from a common ancestor. **e**, The dimeric subunit-*e/g* structures are conserved in pig (PDB 6ZNA) and *T. brucei* (this work) and contain a conserved GXXXG motif (orange) mediating interaction of transmembrane helices. **f**, Models of ATP synthase dimers fitted into subtomogram averages of short oligomers[15] (EMD-3560).

9
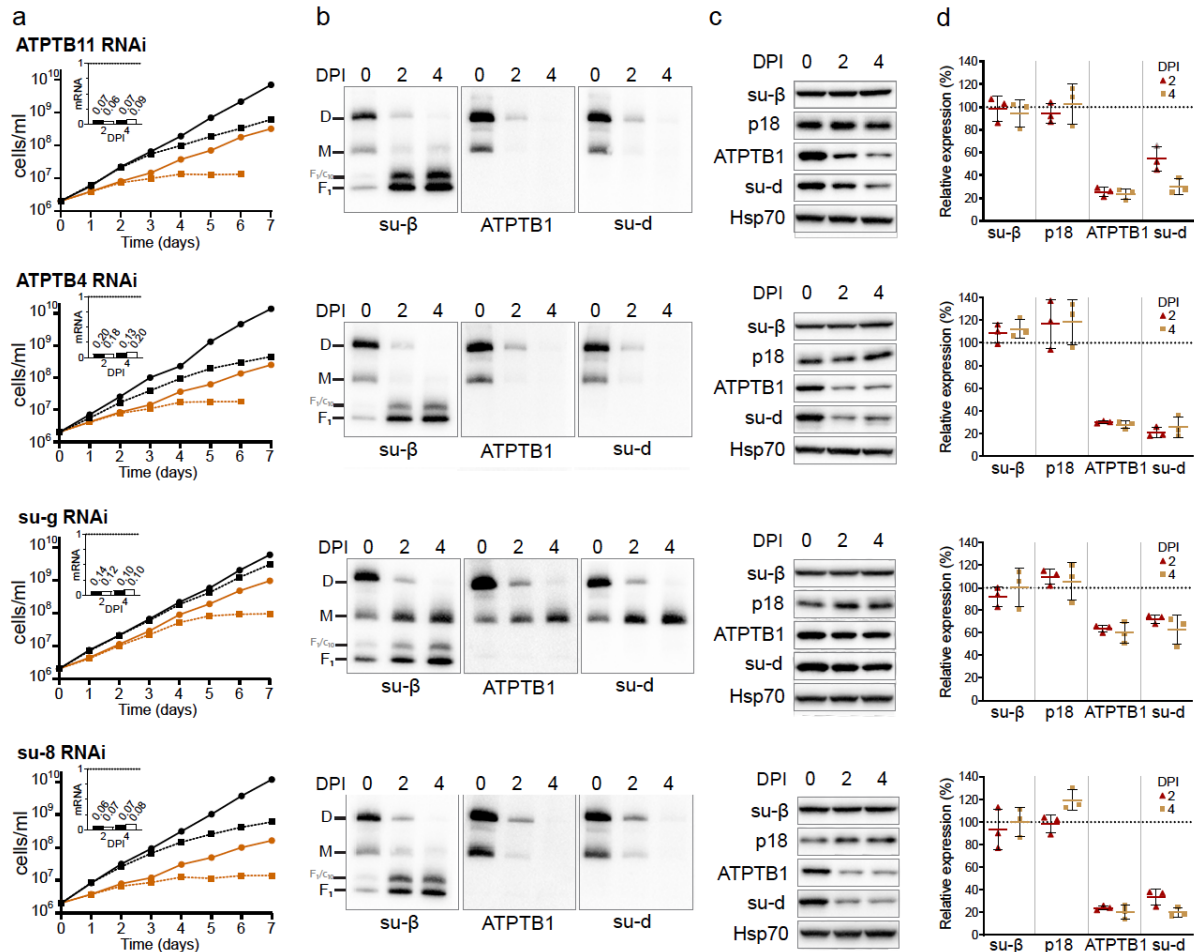
Fig. 6: RNAi knockdown of subunit-*g* results in monomerization of ATP synthase. a, Growth curves of non-induced (solid lines) and tetracycline-induced (dashed lines) RNAi cell lines grown in the presence (black) or absence (brown) of glucose. The insets show relative levels of the respective target mRNA at indicated days post-induction (DPI) normalized to the levels of 18S rRNA (black bars) or ß-tubulin (white bars). **b**, Immunoblots of mitochondrial lysates from indicated RNAi cell lines resolved by BN-PAGE probed with antibodies against indicated ATP synthase subunits. **c**, Representative immunoblots of whole cell lysates from indicated RNAi cell lines probed with indicated antibodies. **d**, Quantification of three replicates of immunoblots in (c). Values were normalized to the signal of loading marker Hsp70 and to non-induced cells. Plots show means with standard deviations (SD).

10

**Subunit-*g* retains the dimer but is not essential for the catalytic monomer**

To validate structural insights, we knocked down each individual F_o subunit by inducible RNA interference (RNAi). All target mRNAs dropped to 5-20 % of their original levels after two and four days of induction (Fig. 6a and Supplementary Fig. 7a, insets). Western blot analysis of whole-cell lysates resolved by denaturing electrophoresis revealed decreased levels of F_o subunits ATPB1 and -*d* suggesting that integrity of F_o moiety depends on the presence of other F_o subunits. Immunoblotting of mitochondrial complexes resolved by blue native polyacrylamide gel electrophoresis (BN-PAGE) with antibodies against F_1 and F_o subunits revealed a strong decrease or nearly complete loss of dimeric and monomeric forms of ATP synthases four days after induction of RNAi of most subunits (*e*, *f*, *i/j*, *k*, 8, ATPTB3, ATPTB4, ATPTB6, ATPTB11, ATPTB12, ATPTB14, ATPEG3 and ATPEG4), documenting an increased instability of the enzyme or defects in its assembly. Simultaneous increase in F_1-ATPase levels demonstrated that the catalytic moiety remains intact after the disruption of the peripheral stalk or the membrane subcomplex (Fig. 6b,c,d and Supplementary Fig. 7b,c,d).

In contrast to the other targeted F_o subunits, the downregulation of subunit-*g* with RNAi resulted in a specific loss of dimeric complexes with concomitant accumulation of monomers (Fig. 6b), indicating that it is required for dimerization, but not for the assembly and stability of the monomeric F_1F_o ATP synthase units. Transmission electron microscopy of thin cell sections revealed that the ATP synthase monomerization in the subunit-*g*[RNAi] cell line had the same effect on mitochondrial ultrastructure as nearly complete loss of monomers and dimers upon knockdown of subunit-8. Both cell lines exhibited decreased cristae counts and aberrant cristae morphology (Fig. 7a,b), including the appearance of round shapes reminiscent of structures detected upon deletion of subunit-*g* or -*e* in *Saccharomyces cerevisiae*[1]. These results indicate that monomerization prevents the trypanosomal ATP synthase from assembling into short helical rows on the rims of the discoidal cristae[15], as has been reported for impaired oligomerisation in counterparts from other eukaryotes[2,34].

Despite the altered mitochondrial ultrastructure, the subunit-*g*[RNAi] cells showed only a very mild growth phenotype, in contrast to all other RNAi cell lines that exhibited steadily slowed growth from day 3 to 4 after the RNAi induction (Fig. 6a, Supplementary Fig. 7a). This is consistent with the growth defects observed after the ablation of F_o subunit ATPTB1[19] and F_1 subunits-α and p18[12]. Thus, the monomerization of ATP synthase upon subunit-*g* ablation had only a negligible effect on the fitness of trypanosomes cultured in glucose-rich media, in which ATP production by substrate level phosphorylation partially compensates for compromised oxidative phosphorylation[35].

Measurement of oligomycin-sensitive ATP-dependent mitochondrial membrane polarization by safranin O assay in permeabilized cells showed that the proton pumping activity of the ATP synthase in the induced subunit-*g*[RNAi] cells is sufficient to generate mitochondrial membrane potential, demonstrating that the monomerized enzyme is catalytically functional. By contrast, RNAi downregulation of subunit-8, ATPTB4 and ATPTB11, and ATPTB1 resulted in a strong decline of the mitochondrial membrane polarization capacity, consistent with the loss of both monomeric and dimeric ATP synthase forms (Fig. 7c). Accordingly, knockdown of the same subunits resulted in inability to produce ATP by oxidative phosphorylation (Fig. 7d). However, upon subunit-*g* ablation the ATP production was affected only partially, confirming that the

11

monomerized ATP synthase remains catalytically active. The ~50 % drop of ATP production in the subunit-g^{RNAi} cells can be attributed to the decreased oxidative phosphorylation efficiency due to the impaired cristae morphology. Indeed, when cells were cultured in the absence of glucose enforcing the need for oxidative phosphorylation, knockdown of subunit-g results in a growth arrest, albeit one to two days later than knockdown of all other tested subunits (Fig. 6a). The data show that dimerization is critical when oxidative phosphorylation is the predominant source of ATP.
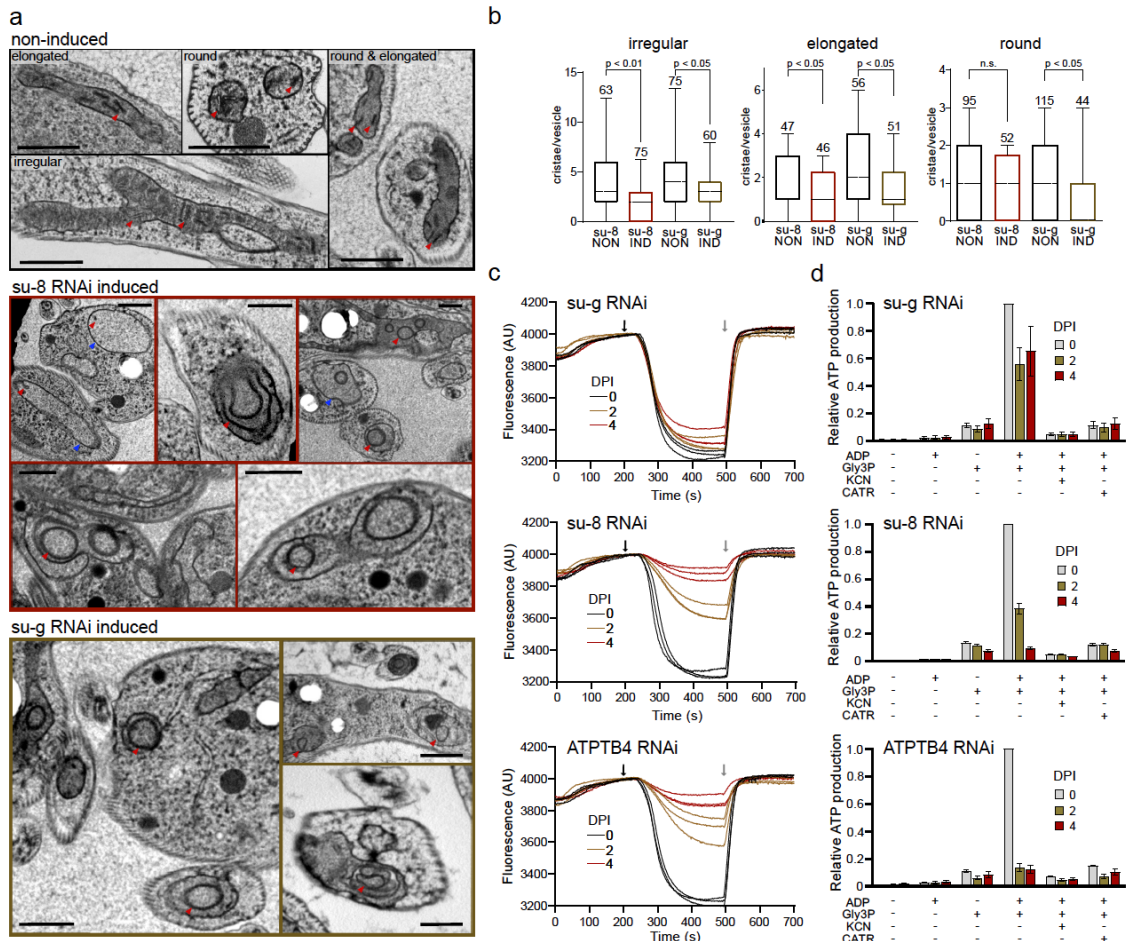
Fig. 7: Monomerization of ATP synthase by subunit-*g* knockdown results in aberrant mitochondrial ultrastructure but does not abolish catalytic activity. a, Transmission electron micrographs of sections of non-induced or 4 days induced RNAi cell lines. Mitochondrial membranes and cristae are marked with blue and red arrowheads, respectively. Top panel shows examples of irregular, elongated and round cross-sections of mitochondria quantified in (b). **b**, Cristae numbers per vesicle from indicated induced (IND) or non-induced (NON) cell lines counted separately in irregular, elongated and round mitochondrial cross-section. Boxes and whiskers show 25th to 75th and 5th to 95th percentiles, respectively. The numbers of analysed cross-sections are indicated for each data point. **c**, Safranin O measurement of ability to generate mitochondrial membrane potential in non-induced or tetracycline-induced RNAi cell lines 2 and 4 DPI. Black and gray arrow indicate addition of ATP and oligomycin, respectively. **d**, ATP production in permeabilized non-induced or tetracycline-induced RNAi cells 2 and 4 DPI in the presence of indicated substrates and inhibitors. Error bars represent SD of four replicates.

12

Discussion

Our structure of the mitochondrial ATP synthase dimer from the mammalian parasite *T. brucei* offers new insight into the mechanism of membrane shaping, catalytic rotation, and proton transfer. Considering that trypanosomes belong to an evolutionarily divergent group of Kinetoplastida, the ATP synthase dimer has several interesting features that differ from other dimer structures. The subunit-*b* found in bacterial and other mitochondrial F-type ATP synthases appears to be highly reduced to a single transmembrane helix *b*H1 represented by a likely homolog ATPTB14. The long *b*H2, which constitutes the central part of the peripheral stalk in other organisms, and is also involved in the composition of the lumenal half proton channel, is completely absent in *T. brucei*. Interestingly, the position of *b*H2 in the proton half channel is occupied by a fully ordered phosphatidylcholine molecule that replaces well-conserved proteinaceous element in the proton path. Lack of the canonical *b*H2 also affects composition of the peripheral stalk in which the divergent subunit-*d* and subunit-*8* binds directly to a C-terminal extension of OSCP, indicating a remodeled peripheral stalk architecture. The peripheral stalk contacts the F_1 headpiece at several positions conferring greater conformational flexibility to the ATP synthase.

Using the structural and functional data, we also identified a conserved structural element of the ATP synthase that is responsible for its multimerization. Particularly, subunit-*g* is required for the dimerization, but dispensable for the assembly of the F_1F_o monomers. Although the monomerized enzyme is catalytically competent, the inability to form dimers results in defective cristae structure, and consequently leads to compromised oxidative phosphorylation and cease of proliferation. The cristae-shaping properties of mitochondrial ATP synthase are critical for sufficient ATP production by oxidative phosphorylation, but not for other mitochondrial functions, as demonstrated by the lack of growth phenotype of subunit-g^{RNAi} cells in the presence of glucose. Thus, trypanosomal subunit-*g* depletion strain represents an experimental tool to assess the roles of the enzyme's primary catalytic function and mitochondria-specific membrane-shaping activity, highlighting the importance of the latter for oxidative phosphorylation.

Based on our data and previously published structures, we propose an ancestral state with double rows of ATP synthase monomers connected by *e/g* modules longitudinally and by other F_o subunits transversally. During the course of evolution, different pairs of adjacent ATP synthase monomer units formed stable dimers in individual lineages (Fig. 8). This gave rise to the highly divergent type-I and type-IV ATP synthase dimers with subunit-*e/g* modules serving as dimerization or oligomerization motives, respectively. Because trypanosomes belong to the deep-branching eukaryotic supergroup Discoba, the proposed arrangement might have been present in the last eukaryotic common ancestor. Although sequence similarity of subunit-*g* is low and restricted to the single transmembrane helix, we found homologs of subunit-*g* in addition to Opisthokonta and Discoba also in Archaeplastida and Amoebozoa, which represent other eukaryotic supergroups, thus supporting the ancestral role in oligomerization (Supplementary Fig. 8). Taken together, our analysis reveals that mitochondrial ATP synthases that display markedly diverged architecture share the ancestral structural module that promotes oligomerization.
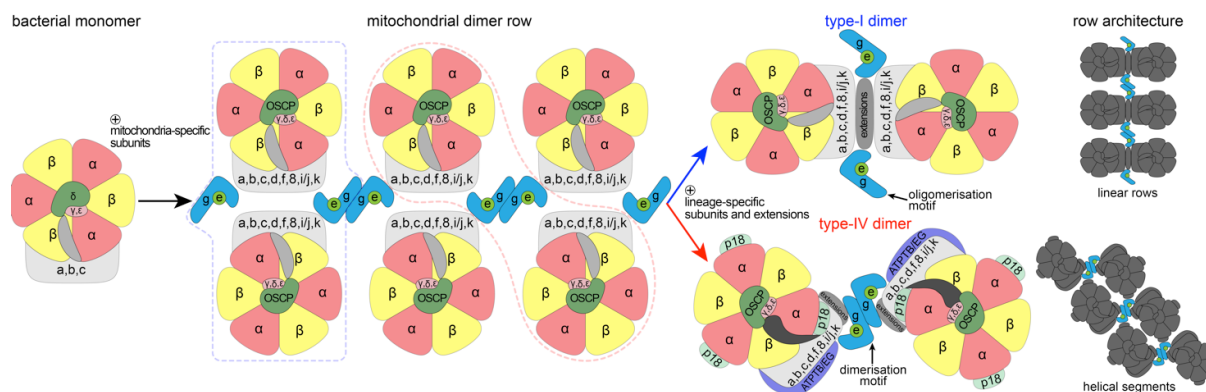
13

Fig. 8: The subunit-*e/g* module is an ancestral oligomerization motif of ATP synthase.
Schematic model of the evolution of type-I and IV ATP synthases. Mitochondrial ATP synthases are derived from a monomeric complex of proteobacterial origin. In a mitochondrial ancestor, acquisition of mitochondria-specific subunits, including the subunit-*e/g* module resulted in the assembly of ATP synthase double rows, the structural basis for cristae biogenesis. Through divergence, different ATP synthase dimer architectures evolved, with the subunit-*e/g* module functioning as an oligomerization (type I) or dimerization (type IV) motif, resulting in distinct row assemblies between mitochondrial lineages.

Materials and Methods

Cell culture and isolation of mitochondria

T. brucei procyclic strains were cultured in SDM-79 medium supplemented with 10% (v/v) fetal bovine serum. For growth curves in no glucose conditions, cells were grown in SDM-80 medium with 10 % dialysed FBS. RNAi cell lines were grown in presence of 2.5 µg/ml phleomycin and 1 µg/ml puromycin. For ATP synthase purification, mitochondria were isolated from the Lister strain 427. Typically, 1.5×10^{11} cells were harvested, washed in 20 mM sodium phosphate buffer pH 7.9 with 150 mM NaCl and 20 mM glucose, resuspended in hypotonic buffer 1 mM Tris-HCl pH 8.0, 1 mM EDTA, and disrupted by 10 strokes in 40 ml Dounce homogenizer. The lysis was stopped by immediate addition of sucrose to 0.25 M. Crude mitochondria were pelleted (15 min at 16,000 xg, 4°C), resuspended in 20 mM Tris-HCl pH 8.0, 250 mM sucrose, 5 mM $MgCl_2$, 0.3 mM $CaCl_2$ and treated with 5 µg/ml DNase I. After 60 min on ice, one volume of the STE buffer (20 mM Tris-HCl pH 8.0, 250 mM sucrose, 2 mM EDTA) was added and mitochondria were pelleted (15 min at 16000 xg, 4°C). The pellet was resuspended in 60% (v/v) Percoll in STE and loaded on six linear 10-35% Percoll gradients in STE in polycarbonate tubes for SW28 rotor (Beckman). Gradients were centrifuged for 1 h at 24,000 rpm, 4°C. The middle phase containing mitochondrial vesicles (15-20 ml per tube) was collected, washed twice in the STE buffer, and pellets were snap-frozen in liquid nitrogen and stored at -80°C.

Plasmid construction and generation of RNAi cell lines

To downregulate ATP synthase subunits by RNAi, DNA fragments corresponding to individual target sequences were amplified by PCR from Lister 427 strain genomic DNA using

14

425 forward and reverse primers extended with restriction sites *Xho*I&*Kpn*I and *Xba*I&*Bam*HI,
426 respectively (Supplementary Table 3). Each fragment was inserted into the multiple cloning
427 sites 1 and 2 of pAZ0055 vector, derived from pRP[HYG-iSL] (courtesy of Sam Alsford) by
428 replacement of hygromycine resistance gene with phleomycine resistance gene, with restriction
429 enzymes *Kpn*I/*Bam*HI and *Xho*I/*Xba*I, respectively. Resulting constructs with tetracycline
430 inducible T7 polymerase driven RNAi cassettes were linearized with *Not*I and transfected into
431 a cell line derived from the Lister strain 427 by integration of the SmOx construct for
432 expression of T7 polymerase and the tetracycline repressor[36] into the β-tubulin locus. RNAi
433 was induced in selected semi-clonal populations by addition of 1 μg/ml tetracycline and the
434 downregulation of target mRNAs was verified by quantitative RT-PCR 2- and 4-days post
435 induction. The total RNA isolated by RNeasy Mini Kit (Qiagen) was treated with 2 μg of
436 DNase I, and then reverse transcribed to cDNA with TaqMan Reverse Transcription kit
437 (Applied Biosciences). qPCR reactions were set with Light Cycler 480 SYBR Green I Master
438 mix (Roche), 2 μl of cDNA and 0.3 μM primers (Supplementary Table 3), and run on
439 LightCycler 480 (Roche). Relative expression of target genes was calculated using - $\Delta\Delta$Ct
440 method with 18S rRNA or β-tubulin as endogenous reference genes and normalized to
441 noninduced cells.

442

443 <u>Denaturing and blue native polyacrylamide electrophoresis and immunoblotting</u>

444 Whole cell lysates for denaturing sodium dodecyl sulphate polyacrylamide electrophoresis
445 (SDS-PAGE) were prepared from cells resuspended in PBS buffer (10 mM phosphate buffer,
446 130 mM NaCl, pH 7.3) by addition of 3x Laemmli buffer (150 mM Tris pH 6.8, 300 mM 1,4-
447 dithiothreitol, 6% (w/v) SDS, 30% (w/v) glycerol, 0.02% (w/v) bromophenol blue) to final
448 concentration of 1×10^7 cells in 30 μl. The lysates were boiled at 97ºC for 10 min and stored at
449 -20ºC. For immunoblotting, lysates from 3×10^6 cells were separated on 4-20 % gradient Tris-
450 glycine polyacrylamide gels (BioRad 4568094), electroblotted onto a PVDF membrane (Pierce
451 88518), and probed with respective antibodies (Supplementary Table 4). Membranes were
452 incubated with the Clarity Western ECL substrate (BioRad 1705060EM) and
453 chemiluminescence was detected on a ChemiDoc instrument (BioRad). Band intensities were
454 quantified densitometrically using the ImageLab software. The levels of individual subunits
455 were normalized to the signal of mtHsp70.

456 Blue native PAGE (BN-PAGE) was performed as described earlier[12] with following
457 modifications. Crude mitochondrial vesicles from 2×10^8 cells were resuspended in 1 M ε-
458 aminocaproic acid (ACA) and solubilized with 2% (w/v) dodecylmaltoside (DDM) for 1 h on
459 ice. Lysates were cleared at 16,000 g for 30 min at 4ºC and their protein concentration was
460 estimated using bicinchoninic acid assay and diluted to 0.25 μg/ μl. 16 μl of each sample was
461 mixed with 2 μl of 50 % (w/v) glycerol and 1.5 μl of loading dye (500 mM ACA, 5% (w/v)
462 Coomassie Brilliant Blue G-250) and resolved on Native PAGE 3-12% Bis-Tris gels
463 (Invitrogen). After the electrophoresis (3 h, 140 V, 4°C), proteins were transferred by
464 electroblotting onto a PVDF membrane (2 h, 100 V, 4ºC, stirring), followed by
465 immunodetection with an appropriate antibody (Supplementary Table 4).

466

467

Mitochondrial membrane potential measurement

Mitochondrial membrane potential was determined fluorometrically employing safranin O dye (Sigma S2255) in permeabilized cells. For each sample, $2x10^7$ cells were harvested and washed with ANT buffer (8 mM KCl, 110 mM K-gluconate, 10 mM NaCl, 10 mM free-acid Hepes, 10 mM K_2HPO_4, 0.015 mM EGTA potassium salt, 10 mM mannitol, 0.5 mg/ml fatty acid-free BSA, 1.5 mM $MgCl_2$, pH 7.25). The cells were permeabilized by 4 μM digitonin in 2 ml of ANT buffer containing 5 μM safranin O. Fluorescence was recorded for 700 s in a Hitachi F-7100 spectrofluorimeter (Hitachi High Technologies) at a 5-Hz acquisition rate, using 495 nm and 585 nm excitation and emission wavelengths, respectively. 1 mM ATP (PanReac AppliChem A1348,0025) and 10 μg/ml oligomycin (Sigma O4876) were added after 200 s and 500 s, respectively. Final addition of the uncoupler SF 6847 (250 nM; Enzo Life Sciences BML-EI215-0050) served as a control for maximal depolarization. All experiments were performed at room temperature and constant stirring.

481

ATP production assay

ATP production in digitonin-isolated mitochondria was performed as described previously[37]. Briefly, $1x10^8$ cells per time point were lysed in SoTE buffer (600 mM sorbitol, 2 mM EDTA, 20 mM Tris-HCl, pH 7.75) containing 0.015% (w/v) digitonin for 5 min on ice. After centrifugation (3 min, 4,000 g, 4ºC), the soluble cytosolic fraction was discarded and the organellar pellet was resuspended in 75 μl of ATP production assay buffer (600 mM sorbitol, 10 mM $MgSO_4$, 15 mM potassium phosphate buffer pH 7.4, 20 mM Tris-HCl pH 7.4, 2.5 mg/ml fatty acid-free BSA). ATP production was induced by addition of 20 mM DL-glycerol phosphate (sodium salt) and 67 μM ADP. Control samples were preincubated with the inhibitors potassium cyanide (1 mM) and carboxyatractyloside (6.5 μM) for 10 min at room temperature. After 30 min at room temperature, the reaction was stopped by addition of 1.5 μl of 70% perchloric acid. The concentration of ATP was estimated using the Roche ATP Bioluminescence Assay Kit HS II in a Tecan Spark plate reader. The luminescence values of the RNAi induced samples were normalized to that of the corresponding noninduced sample.

496

Thin sectioning and transmission electron microscopy

The samples were centrifuged and pellet was transferred to the specimen carriers which were completed with 20% BSA and immediately frozen using high pressure freezer Leica EM ICE (Leica Microsystems). Freeze substitution was performed in the presence of 2% osmium tetroxide diluted in 100% acetone at -90°C. After 96 h, specimens were warmed to -20°C at a slope 5 °C/h. After next 24 h, the temperature was increased to 3°C (3°C/h). In room temperature, samples were washed in acetone and infiltrated with 25%, 50%, 75% acetone/resin EMbed 812 (EMS) mixture 1 h at each step. Finally, samples were infiltrated in 100% resin and polymerized at 60°C for 48h. Ultrathin sections (70 nm) were cut using diamond knife, placed on cupper grids and stained with uranyl acetate and lead citrate. TEM micrographs were taken with Mega View III camera (SIS) using a JEOL 1010 TEM operating at an accelerating voltage of 80 kV.

509

<u>Purification of *T. brucei* ATP synthase dimers</u>

510

511 Mitochondria from 3×10^{11} cells were lysed by 1 % (w/v) DDM in 60 ml of 20 mM Bis-tris

512 propane pH 8.0 with 10 % glycerol and EDTA-free Complete protease inhibitors (Roche) for

513 20 min at 4ºC. The lysate was cleared by centrifugation at 30,000g for 20 min at 4ºC and

514 adjusted to pH 6.8 by drop-wise addition of 1 M 3-(N-morpholino) propanesulfonic acid pH

515 5.9. Recombinant $TbIF_1$ without dimerization region, whose affinity to F_1-ATPase was

516 increased by N-terminal truncation and substitution of tyrosine 36 with tryptophan[20], with a C-

517 terminal glutathione S-transferase (GST) tag ($TbIF_1$(9-64)-Y36W-GST) was added in

518 approximately 10-fold molar excess over the estimated content of ATP synthase. Binding of

519 $TbIF_1$ was facilitated by addition of neutralized 2 mM ATP with 4 mM magnesium sulphate.

520 After 5 min, sodium chloride was added to 100 mM, the lysate was filtered through a 0.2 μm

521 syringe filter and immediately loaded on 5 ml GSTrap HP column (Cytiva) equilibrated in 20

522 mM Bis-Tris-Propane pH 6.8 binding buffer containing 0.1 % (w/v) glyco-diosgenin (GDN;

523 Avanti Polar Lipids), 10 % (v/v) glycerol, 100 mM sodium chloride, 1 mM tris(2-

524 carboxyethyl)phosphine (TCEP), 1 mM ATP, 2 mM magnesium sulphate, 15 ug/ml

525 cardiolipin, 50 ug/ml 1-palmitoyl-2-oleoyl-sn-glycero-3-phosphocholine (POPC), 25 ug/ml 1-

526 palmitoyl-2-oleoyl-sn-glycero-3-phosphoethanolamine (POPE) and 10 ug/ml 1-palmitoyl-2-

527 oleoyl-sn-glycero-3-[phospho-rac-(1-glycerol)] (POPG). All phospholipids were purchased

528 from Avanti Polar Lipids (catalog numbers 840012C, 850457C, 850757C and 840757,

529 respectively). ATP synthase was eluted with a gradient of 20 mM reduced glutathione in Tris

530 pH 8.0 buffer containing the same components as the binding buffer. Fractions containing ATP

531 synthase were pooled and concentrated to 150 μl on Vivaspin centrifugal concentrator with 30

532 kDa molecular weight cut-off. The sample was fractionated by size exclusion chromatography

533 on a Superose 6 Increase 3.2/300 GL column (Cytiva) equilibrated in a buffer containing 20

534 mM Tris pH 8.0, 100 mM sodium chloride, 2 mM magnesium chloride, 0.1 % (w/v) GDN,

535 3.75 ug/ml cardiolipin, 12.5 ug/ml POPC, 6.25 ug/ml POPE and 2.5 ug/ml POPG at 0.03

536 ml/min. Fractions corresponding to ATP synthase were pooled, supplemented with 0.05%

537 (w/v) DDM that we and others experimentally found to better preserve dimer assemblies in

538 cryo-EM[38], and concentrated to 50 ul.

539

<u>Preparation of cryo-EM grids and data collection</u>

540

541 Samples were vitrified on glow-discharged Quantifoil R1.2/1.3 Au 300-mesh grids after

542 blotting for 3 s by plunging into liquid ethane using a Vitrobot Mark IV. 5,199 movies were

543 collected using EPU 1.9 on a Titan Krios (ThermoFisher Scientific) operated at 300 kV at a

544 nominal magnification of 165 kx (0.83 Å/pixel) with a Quantum K2 camera (Gatan) using a

545 slit width of 20 eV. Data was collected with an exposure rate of 3.6 electrons/px/s, a total

546 exposure of 33 electrons/$Å^2$ and 20 frames per movie.

547

<u>Image processing</u>

548

549 Image processing was performed within the Scipion 2 framework[39], using RELION-3.0 unless

550 specified otherwise. Movies were motion-corrected using the RELION implementation of the

17

551 MotionCor2. 294,054 particles were initially picked using reference-based picking in
552 Gautomatch (http://www.mrc-lmb.cam.ac.uk/kzhang/Gautomatch) and Contrast-transfer
553 function parameters were using GCTF[40]. Subsequent image processing was performed in
554 RELION-3.0 and 2D and 3D classification was used to select 100,605 good particles, which
555 were then extracted in an unbinned 560-pixel box (Fig. S1). An initial model of the ATP
556 synthase dimer was obtained using *de novo* 3D model generation. Using masked refinement
557 with applied C_2 symmetry, a 2.7-Å structure of the membrane region was obtained following
558 per-particle CTF refinement and Bayesian polishing. Following C_2-symmetry expansion and
559 signal subtraction of one monomer, a 3.7 Å of the peripheral stalk was obtained. Using 3D
560 classification (T=100) of aligned particles, with a mask on the F_1/c-ring region, 10 different
561 rotational substates were then separated and maps at 3.5-4.3 Å resolution were obtained using
562 3D refinement. The authors note that the number of classes identified in this study likely
563 reflects the limited number of particles, rather than the complete conformational space of the
564 complex. By combining particles from all states belonging to main rotational state 1, a 3.7-Å
565 map of the rotor and a 3.2-Å consensus map of the complete ATP synthase dimer with both
566 rotors in main rotational state 1.

568 <u>Model building, refinement and data visualisation</u>

569 An initial atomic model of the static F_o membrane region was automatically built using
570 Bucaneer[41]. Subunits were subsequently assigned directly from the cryo-EM map, 15 of them
571 corresponding to previously identified *T. brucei* ATP synthase subunits[21], while three subunits
572 (ATPTB14, ATPEG3, ATPEG4) were newly identified using BLAST searches. Manual model
573 building was performed in *Coot* using the *T. brucei* F_1 (PDB 6F5D) and homology models[42] of
574 the *E. gracilis* OSCP and *c*-ring (PDB 6TDU) as starting models. Ligands were manually fitted
575 to the map and restraints were generated by the GRADE server (http://grade.globalphasing.org)
576 Real-space refinement was performed in PHENIX using auto-sharpened, local-resolution-
577 filtered maps of the membrane region, peripheral stalk tip, *c*-ring/central stalk and F_1F_o
578 monomers in different rotational states, using secondary structure restraints. Model statistics
579 were generated using MolProbity and EMRinger. Finally, the respective refined models were
580 combined into a composite ATP synthase dimer model and real-space refined against the local-
581 resolution-filtered consensus ATP synthase dimer map with both monomers in rotational state
582 1, applying reference restraints. Figures of the structures were prepared using ChimeraX[43], the
583 proton half channels were traced using HOLLOW[44].

585 **Data availability**

586 The atomic coordinates have been deposited in the Protein Data Bank (PDB) and are available
587 under the accession codes: XXX (membrane-region), XXX (peripheral stalk), XXX (rotor),
588 XXX (F1Fo dimer), XXX (rotational state 1a), XXX (rotational state 1b), XXX (rotational
589 state 1c), XXX (rotational state 1d), XXX (rotational state 1e), XXX (rotational state 2a), XXX
590 (rotational state 2b), XXX (rotational state 2c), XXX (rotational state 2d), XXX (rotational
591 state 3). The local resolution filtered cryo-EM maps, half maps, masks and FSC-curves have
592 been deposited in the Electron Microscopy Data Bank with the accession codes: EMD-XXX
593 (membrane-region), EMD-XXX (peripheral stalk), EMD-XXX (rotor), EMD-XXX (F_1F_o

18

dimer), EMD-XXX (rotational state 1a), EMD-XXX (rotational state 1b), EMD-XXX (rotational state 1c), EMD-XXX (rotational state 1d), EMD-XXX (rotational state 1e), EMD-XXX (rotational state 2a), EMD-XXX (rotational state 2b), EMD-XXX (rotational state 2c), EMD-XXX (rotational state 2d), EMD-XXX (rotational state 3).

References

1. Paumard, P. et al. The ATP synthase is involved in generating mitochondrial cristae morphology. *EMBO J* **21**, 221-30 (2002).
2. Davies, K.M., Anselmi, C., Wittig, I., Faraldo-Gomez, J.D. & Kuhlbrandt, W. Structure of the yeast F_1F_o-ATP synthase dimer and its role in shaping the mitochondrial cristae. *Proc Natl Acad Sci U S A* **109**, 13602-7 (2012).
3. Panek, T., Elias, M., Vancova, M., Lukes, J. & Hashimi, H. Returning to the Fold for Lessons in Mitochondrial Crista Diversity and Evolution. *Curr Biol* **30**, R575-R588 (2020).
4. Kuhlbrandt, W. Structure and Mechanisms of F-Type ATP Synthases. *Annu Rev Biochem* **88**, 515-549 (2019).
5. Spikes, T.E., Montgomery, M.G. & Walker, J.E. Structure of the dimeric ATP synthase from bovine mitochondria. *Proc Natl Acad Sci U S A* **117**, 23519-23526 (2020).
6. Pinke, G., Zhou, L. & Sazanov, L.A. Cryo-EM structure of the entire mammalian F-type ATP synthase. *Nat Struct Mol Biol* **27**, 1077-1085 (2020).
7. Guo, H., Bueler, S.A. & Rubinstein, J.L. Atomic model for the dimeric F_o region of mitochondrial ATP synthase. *Science* **358**, 936-940 (2017).
8. Murphy, B.J. et al. Rotary substates of mitochondrial ATP synthase reveal the basis of flexible F_1-F_o coupling. *Science* **364**, eaaw9128 (2019).
9. Flygaard, R.K., Mühleip, A., Tobiasson, V. & Amunts, A. Type III ATP synthase is a symmetry-deviated dimer that induces membrane curvature through tetramerization. *Nature Communications* **11**, 5342 (2020).
10. Muhleip, A., McComas, S.E. & Amunts, A. Structure of a mitochondrial ATP synthase with bound native cardiolipin. *Elife* **8**, e51179 (2019).
11. Mühleip, A. et al. ATP synthase hexamer assemblies shape cristae of *Toxoplasma* mitochondria. *Nature Communications* **12**, 120 (2021).
12. Gahura, O. et al. The F_1-ATPase from *Trypanosoma brucei* is elaborated by three copies of an additional p18-subunit. *FEBS J* **285**, 614-628 (2018).
13. Montgomery, M.G., Gahura, O., Leslie, A.G.W., Zikova, A. & Walker, J.E. ATP synthase from *Trypanosoma brucei* has an elaborated canonical F_1-domain and conventional catalytic sites. *Proc Natl Acad Sci U S A* **115**, 2102-2107 (2018).
14. Serricchio, M. et al. Depletion of cardiolipin induces major changes in energy metabolism in *Trypanosoma brucei* bloodstream forms. *FASEB J* **35, 21176** (2020).
15. Muhleip, A.W., Dewar, C.E., Schnaufer, A., Kuhlbrandt, W. & Davies, K.M. In situ structure of trypanosomal ATP synthase dimer reveals a unique arrangement of catalytic subunits. *Proc Natl Acad Sci U S A* **114**, 992-997 (2017).

19

16. Schnaufer, A., Clark-Walker, G.D., Steinberg, A.G. & Stuart, K. The F_1-ATP synthase complex in bloodstream stage trypanosomes has an unusual and essential function. *EMBO J* **24**, 4029-40 (2005).

17. Brown, S.V., Hosking, P., Li, J. & Williams, N. ATP synthase is responsible for maintaining mitochondrial membrane potential in bloodstream form *Trypanosoma brucei*. *Eukaryot Cell* **5**, 45-53 (2006).

18. Gahura, O., Hierro-Yap, C. & Zikova, A. Redesigned and reversed: Architectural and functional oddities of the trypanosomal ATP synthase. *Parasitology* **148**, 1151-1160 (2021).

19. Hierro-Yap, C. et al. Bioenergetic consequences of F_oF_1-ATP synthase/ATPase deficiency in two life cycle stages of *Trypanosoma brucei*. *J Biol Chem* **296**, 100357 (2021).

20. Gahura, O., Panicucci, B., Vachova, H., Walker, J.E. & Zikova, A. Inhibition of F_1-ATPase from *Trypanosoma brucei* by its regulatory protein inhibitor TbIF1. *FEBS J* **285**, 4413-4423 (2018).

21. Zikova, A., Schnaufer, A., Dalley, R.A., Panigrahi, A.K. & Stuart, K.D. The F(0)F(1)-ATP synthase complex contains novel subunits and is essential for procyclic *Trypanosoma brucei*. *PLoS Pathog* **5**, e1000436 (2009).

22. Perez, E. et al. The mitochondrial respiratory chain of the secondary green alga *Euglena gracilis* shares many additional subunits with parasitic Trypanosomatidae. *Mitochondrion* **19 Pt B**, 338-49 (2014).

23. Sathish Yadav, K.N. et al. Atypical composition and structure of the mitochondrial dimeric ATP synthase from *Euglena gracilis*. *Biochim Biophys Acta* **1858**, 267-275 (2017).

24. Aphasizheva, I. et al. Lexis and Grammar of Mitochondrial RNA Processing in Trypanosomes. *Trends Parasitol* **36**, 337-355 (2020).

25. Blum, B., Bakalara, N. & Simpson, L. A model for RNA editing in kinetoplastid mitochondria: "guide" RNA molecules transcribed from maxicircle DNA provide the edited information. *Cell* **60**, 189-98 (1990).

26. Adler, B.K., Harris, M.E., Bertrand, K.I. & Hajduk, S.L. Modification of *Trypanosoma brucei* mitochondrial rRNA by posttranscriptional 3' polyuridine tail formation. *Mol Cell Biol* **11**, 5878-84 (1991).

27. Hofer, A., Steverding, D., Chabes, A., Brun, R. & Thelander, L. *Trypanosoma brucei* CTP synthetase: a target for the treatment of African sleeping sickness. *Proc Natl Acad Sci U S A* **98**, 6412-6 (2001).

28. Gupta, K. et al. The role of interfacial lipids in stabilizing membrane protein oligomers. *Nature* **541**, 421-424 (2017).

29. Arnold, I., Pfeiffer, K., Neupert, W., Stuart, R.A. & Schagger, H. Yeast mitochondrial F_1F_o-ATP synthase exists as a dimer: identification of three dimer-specific subunits. *EMBO J* **17**, 7170-8 (1998).

30. Gu, J. et al. Cryo-EM structure of the mammalian ATP synthase tetramer bound with inhibitory protein IF1. *Science* **364**, 1068-1075 (2019).

20

677 31. Spikes, T.E., Montgomery, M.G. & Walker, J.E. Interface mobility between monomers
678   in dimeric bovine ATP synthase participates in the ultrastructure of inner mitochondrial
679   membranes. *Proc Natl Acad Sci U S A* **118**, e2021012118 (2021).
680 32. Cadena, L.R. et al. Mitochondrial contact site and cristae organization system and F_1F_o-
681   ATP synthase crosstalk is a fundamental property of mitochondrial cristae. *mSphere* **6**,
682   e0032721 (2021).
683 33. Davies, K.M. et al. Macromolecular organization of ATP synthase and complex I in
684   whole mitochondria. *Proc Natl Acad Sci U S A* **108**, 14121-6 (2011).
685 34. Blum, T.B., Hahn, A., Meier, T., Davies, K.M. & Kühlbrandt, W. Dimers of
686   mitochondrial ATP synthase induce membrane curvature and self-assemble into rows.
687   *Proc Natl Acad Sci U S A* **116**, 4250-4255 (2019).
688 35. Bochud-Allemann, N. & Schneider, A. Mitochondrial substrate level phosphorylation
689   is essential for growth of procyclic *Trypanosoma brucei*. *J Biol Chem* **277**, 32849-54
690   (2002).
691 36. Poon, S.K., Peacock, L., Gibson, W., Gull, K. & Kelly, S. A modular and optimized
692   single marker system for generating *Trypanosoma brucei* cell lines expressing T7 RNA
693   polymerase and the tetracycline repressor. *Open Biol* **2**, 110037 (2012).
694 37. Allemann, N. & Schneider, A. ATP production in isolated mitochondria of procyclic
695   Trypanosoma brucei. *Mol Biochem Parasitol* **111**, 87-94 (2000).
696 38. Aibara, S., Dienemann, C., & Cramer, P.. Structure of an inactive RNA polymerase II
697   dimer. *Nucleic Acids Research*, gkab783 (2021).
698 39. de la Rosa-Trevin, J.M. et al. Scipion: A software framework toward integration,
699   reproducibility and validation in 3D electron microscopy. *J Struct Biol* **195**, 93-9
700   (2016).
701 40. Zhang, K. Gctf: Real-time CTF determination and correction. *J Struct Biol* **193**, 1-12
702   (2016).
703 41. Cowtan, K. The Buccaneer software for automated model building. 1. Tracing protein
704   chains. *Acta Crystallogr D Biol Crystallogr* **62**, 1002-11 (2006).
705 42. Waterhouse, A. et al. SWISS-MODEL: homology modelling of protein structures and
706   complexes. *Nucleic Acids Res* **46**, W296-W303 (2018).
707 43. Goddard, T.D. et al. UCSF ChimeraX: Meeting modern challenges in visualization and
708   analysis. *Protein Sci* **27**, 14-25 (2018).
709 44. Ho, B.K. & Gruswitz, F. HOLLOW: generating accurate representations of channel
710   and interior surfaces in molecular structures. *BMC Struct Biol* **8**, 49 (2008).
711

Acknowledgements

21

723

Author contributions

725   O.G. prepared the sample for cryo-EM. O.G. and A.M. performed initial screening. A.M.
726   processed the cryo-EM data and built the model. B.P., C.H.Y., M.J., M.S., O.G. and A.Z.
727   performed biochemical analysis. O.G., A.M. and A.A. analyzed the structure. O.G., A.M., A.A.
728   and A.Z. wrote the manuscript. All authors contributed to the analysis and the final version of
729   the manuscript.

730   **SUPPLEMENTARY INFORMATION**

731

732   **Supplementary Videos:**

733

734   **Supplementary Video 1. Overall structure and subunit-e/g module of trypanosomal ATP**
735   **synthase dimers.** Subunits are coloured as in Figure 1. Phospholipids and ligands are shown
736   as sticks.

737

738   **Supplementary Video 2. Rotary cycle of *T. brucei* ATP synthase.** Top view showing
739   flexibility of the peripheral stalk, including bending of its apical part, and rotational and tilting
740   motions of F_1.

741

742   **Supplementary Video 3. Rotary cycle of *T. brucei* ATP synthase.** Side view showing
743   rotational and tilting motions of the F_1/c-ring subcomplex.

744

745

746

747

748

749

750

751

752

753

754

755

756

757

758

759

760

761

762

763

       23

764 **Supplementary Tables:**

765

766 **Supplementary Table 1. List of models and refinement statistics**

	Membrane region	Rotor	Peripheral stalk	F_1F_o dimer	Rot. 1a	Rot. 1b	Rot. 1c	Rot. 1d	Rot. 1e	Rot. 2a	Rot. 2b	Rot. 2c	Rot. 2d	Rot. 3
Data collection														
Microscope	Titan Krios													
Voltage (kV)	300													
Camera	K2 Summit													
Magnification	165 kx													
Exposure ($e^-/\text{Å}^2$)	33													
Defocus range (μm)	-1.6 to -3.2													
Pixel size (Å)	0.83													
Movies collected	5,199													
Frames per movie	20													
Data processing														
Initial particles	100,605 (C_2 symmetry-expanded: 201,210)													
Final no. particles	100,605	118,683	201,210	36,925	19,764	26,427	23,019	16,991	34,482	12,173	24,096	11,035	17,833	17.312
Symmetry	C_2	C_1	C_1	C_2	C_1	C_1	C_1	C_1	C_1	C_1	C_1	C_1	C_1	C_1
Map resolution (Å)	2.7	3.7	3.7	3.2	3.7	3.5	3.7	3.8	3.7	4.3	3.5	3.8	3.8	3.7
Sharpening B factor	-46.2	-74.4	-92.5	-49.8	-61.8	-61.1	-57.6	-45.6	-58.0	-73.8	-54.5	-65.2	-54.9	-61.7
EMD ID														
Model refinement statistics														
CC (map/model)	0.86	0.83	0.82	0.71	0.79	0.79	0.82	0.79	0.69	0.71	0.81	0.77	0.77	0.79
Resolution (map/model)	2.65	3.4	3.68	3.13	3.48	3.56	3.36	3.55	3.57	3.94	3.39	3.73	3.64	3.58
No. of atoms	76,690	19,669	12,083	251,552	129,568	129,568	129,568	129,568	129,568	129,563	129,563	129,563	129,563	129,566
No. of residues	4074	1285	767	15,356	7872	7872	7872	7872	7872	7872	7872	7872	7872	7872
No. of lipids	36	0	0	36	21	21	21	21	21	21	21	21	21	21
No. of ATP/ADP	0	0	0	10	5	5	5	5	5	5	5	5	5	5
No. of Mg ions	0	0	0	10	5	5	5	5	5	5	5	5	5	5
B-factor (Å^2)														
- protein	54.05	56.13	77.88	84.48	55.65	70.37	80.22	83.27	70.70	112,72	79.93	65.52	66.49	101.5
- ligands	50.57	58.25	-	69.94	40.99	72.29	63.18	78.43	63.76	75,25	74.47	61.79	46.55	83.68
Rotamer outliers (%)	0.44	0.40	0.31	0.22	0.42	0.09	0.18	0.26	0.58	0.18	0.27	0.48	0.42	0.39
Ramachandran (%)														
- outliers	0.00	0.00	0.00	0.01	0.001	0.003	0.004	0.01	0.003	0.01	0.00	0.04	0.04	0.04
- allowed	1.57	1.91	1.59	1.56	1.52	1.65	1.44	1.49	1.49	1.67	1.58	1.47	1.65	1.79
- favored	98.43	98.08	98.41	98.42	98.47	98.34	98.56	98.49	98.48	98.31	98.42	98.49	98.31	98.17
Clash score	1.66	2.44	2.32	2.26	2.60	2.65	2.53	2.67	2.99	2.38	2.30	2.52	2.38	3.57
MolProbity score	0.92	1.03	1.01	1.00	1.05	1.05	1.04	1.05	1.09	1.02	1.01	1.04	1.02	1.15
RMSD														
- bonds (Å)	0.004	0.004	0.02	0.003	0.003	0.003	0.004	0.003	0.003	0.002	0.003	0.003	0.003	0.003
- angles (°)	0.455	0.416	0.386	0.407	0.414	0.424	0.417	0.407	0.412	0.410	0.416	0.419	0.428	0.421
EMRinger score	5.11	3.96	1.61	2.56	3.24	2.95	3.32	2.85	3.32	1.35	2.89	2.32	2.49	2.8
PDB ID														

768

769

24

Supplementary Table 2. Composition of *T. brucei* ATP synthase dimer

Subunit name	TriTrypDB Lister strain 427 ID	TriTrypDB TREU927 strain ID	Uniprot TREU927 strain ID	Residues	Residues built
F₁ subcomplex					
α	Tb427_070081800 Tb427_070081900	Tb927.7.7420 Tb927.7.7430	Q57TX9	584	45-151, 161-584
β	Tb427_030013500	Tb927.3.1380	Q57XX1	519	26-514
γ	Tb427_100005200	Tb927.10.180	B0Z0F6	305	2-301
δ	Tb427_060054900	Tb927.6.4990	Q586H1	182	22-182
ε	Tb427_100054600	Tb427.10.5050	N/A	75	11-75
p18	Tb427_050022900	Tb927.5.1710	Q57ZP0	188	23-188
Fₒ subcomplex					
OSCP	Tb427_100087100	Tb927.10.8030	Q38AG1	255	18-202, 208-255
a	mt encoded	mt encoded	N/A	231	1-231
c	Tb427_100018700 Tb427_110057900 Tb427_070019000	Tb927.10.1570 Tb927.11.5280 Tb927.7.1470	Q38C84 Q385P0 Q57WQ3	118	41-118
d	Tb427_050035800	Tb927.5.2930	Q57ZW9	370	17-325, 332-354
e	Tb427_110010200	Tb927.11.600	N/A	92	1-383
f	Tb427_030016600	Tb927.3.1690	Q57ZE2	145	2-136
g	Tb427_020016900	Tb927.2.3610	Q586X8	144	16-144
i/j	Tb427_030029400	Tb927.3.2880	Q57ZM4	104	2-104
k	Tb427_070011800	Tb927.7.840	Q57VT0	124	20-124
8	Tb427_040037300	Tb927.4.3450	Q585K5	114	29-114
ATBTB1	Tb427_100008400	Tb927.10.520	Q38CI8	396	1-383
ATPTB3	Tb427_110067400	Tb927.11.6250	Q385E4	269	2-269
ATPTB4	Tb427_100105100	Tb927.10.9830	Q389Z3	157	21-157
ATPTB6	Tb427_110017200	Tb927.11.1270	Q387C5	169	2-169
ATPTB11	Tb427_030021500	Tb927.3.2180	Q582T1	156	18-156
ATPTB12	Tb427_050037400	Tb927.5.3090	Q57Z84	101	5-100
ATPTB14	Tb427_040009100	Tb927.4.720	Q580A0	105	26-105
ATPEG3	Tb427_060009300	Tb927.6.590	Q583U4	98	14-98
ATPEG4	N/A	Tb927.11.2245	N/A	62	1-62

25

773 **Supplementary Table 3. List of oligonucleotides**

Subunit	Primer pair sequences
Primers for amplification of RNAi cassettes	
e	TAATCTCGAGGGTACCGGGAGTACAGAAGGGCTACA TAGATCTAGAGGATCCCGTGCACACCATCAGCTG
f	ATACTCGAGGGTACCGTGAGTACCGCCTTTACGC GCGTCTAGAGGATCCAGCACTGATCACCAAACTGC
g	ACTGCTCGAGGGTACCACGCGGGAATTCAAAAGACC GCGGTCTAGAGGATCCCGTTGCGGTGCTTGTCATTA
i/j	TAATCTCGAGGGTACCGAATATCCGATGCATGCCGC GCCGTCTAGAGGATCCACTTCGCTCTACTGCATGCA
k	ATTACTCGAGCCCGGGCGATCAGTGCAGGGGATTTT GCCGTCTAGAGGATCCTTTCCTCGAAAACGCACACA
8	ATGACTCGAGGGTACCGGGCTATGGTGTGGTATTATGC GACGTCTAGAGGATCCGCAGAAAACTCCCAACGACA
ATPTB3	ACTGCTCGAGGGTACCAAAGAGGAGGTGAGGTCTGC GCAGTCTAGAGGATCCCCCCTAGGGTTCTTCGAAGCA
ATPTB4	CTGACTCGAGGGTACCTTCCTTTTCTGCTGCATCGG GCAGTCTAGAGGATCCCTCCTCGGGCTTCCAATTTG
ATPTB6	ACTGCTCGAGGGTACCCAACATGGCAGTATCCGGTG GCAGTCTAGAGGATCCTTATTAGTGGCGGTGGTGGT
ATPTB11	ACTGCTCGAGGGTACCGCGCTCGTCTTCTCCATTTC GCAGAAGCTTGGATCCAGGTTGGGGTGTTTAGGGAG
ATPTB12	TAATCTCGAGGGTACCGACGCCATCAAAGGAATGCC GCCGTCTAGAGGATCCAGCAGCCAACAAACAGACAA
ATPTB14	TAATCTCGAGGGTACCGTTGAGTGAGGAGGAACGGG GCAGTCTAGAGGATCCTATCCCTTCCACCCACCACT
ATPEG3	TACACTCGAGGGTACCAAACCTGAAGGCCCTCACAC GCAGTCTAGAGGATCCCTCTTTCGTGCCGCCTGATA
Primers for quantification of mRNA levels by qPCR	
e	CAAGCCTTGCACACACTTTATG CCGCAAAGAAGTACGCCAC
f	TTTTCTACATACCGCAGCAGT TACCATTCCATGCGCGTTG
g	GCAATTGTGTGAGCTGAACG TACTGGCCGCATTGCATAAC
i/j	AGAGTAAAAGCGCGCCTACG CAGTTGGAAAACCGGTAGCC
k	ACACAAAACACTTCCAGCAGA

26

		CGCTATGACGGACAGGTGT
8		GCTACGGCGACTTGGTGC
		CGTCACCGCGTATTTGTTCA
ATPTB3		AACGTTTATATCAGCGGGCG
		CTGTTTTGGTCTGCACACGA
ATPTB4		CCAAACTTTGAAGCAGCGGA
		ATTCCTTGGATCCGCACCTT
ATPTB6		TCGGCATAGGAGAAGTAACGA
		GATTCGGTTTGGAACTTGCG
ATPTB11		CAACGGCCCCACATTCTC
		ACACCGCGGTCATTCATTG
ATPTB12		GCACTTCATTCTCCCGACTG
		ACATGATGTAACACCTCCGC
ATPTB14		CCAAGAGTGATGATGGCCCC
		CGTTTAGGGTCGCGGAAAAC
ATPEG3		TGGCCCCACATGACTGAAAA
		GGAAGTGATCCGCCGGATTT

774

775

776

777

778

779

780

781

782

783

784

785

786

787

788

789

790

791

792

27

793   **Supplementary Table 4. List of antibodies used in this study**

Target	Type	Reference	Dilution SDS-PAGE	Dilution BN-PAGE
Primary antibodies				
subunit-β	rabbit polyclonal	1	1:2000	1:2000
p18	rabbit polyclonal	1	1:1000	-
ATPTB1	rabbit polyclonal	1	1:1000	1:1000
subunit-*d*	rabbit polyclonal	1	1:1000	1:500
mtHsp70	mouse monoclonal	2	1:5000	-
Secondary antibodies				
goat anti-rabbit IgG HRP conjugate	BioRad 1721019		1:2000	1:2000
goat anti-mouse IgG HRP conjugate	BioRad 1721011		1:2000	1:2000

794

28

Supplementary Figures:
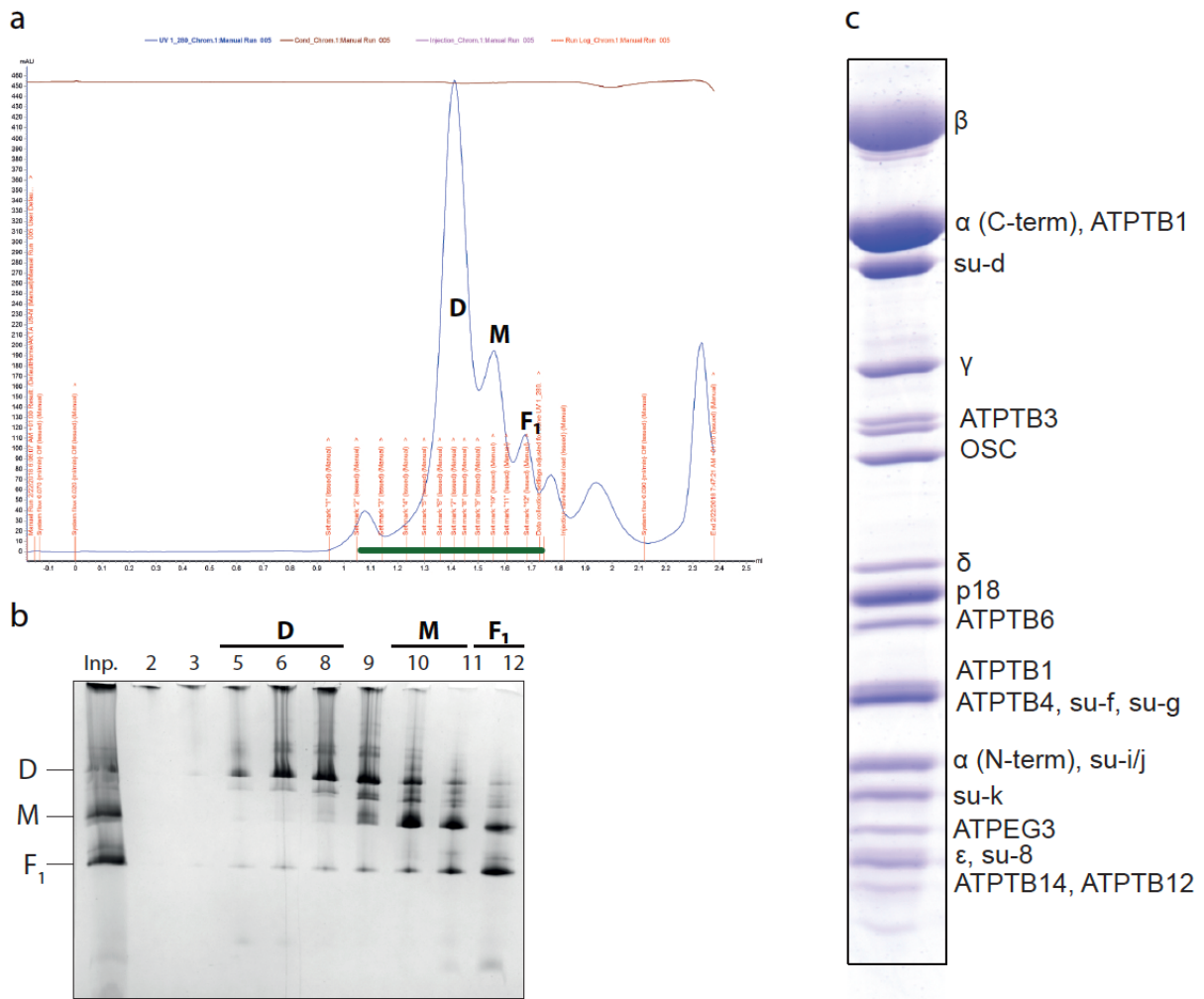
Supplementary figure 1: Purification of the *T. brucei* ATP synthase dimer. a, Size exclusion chromatography trace with peaks enriched with ATP synthase dimers (D), monomers (M) and F_1-ATPase (F_1) labelled. **b,** Fractions from size exclusion chromatography marked with green bar in (a) resolved by native BN-PAGE. **c,** Dimer-enriched fraction resolved by SDS-PAGE stained by Coomassie blue dye. Bands are annotated based on mass spectrometry identification from excised gel pieces.

29
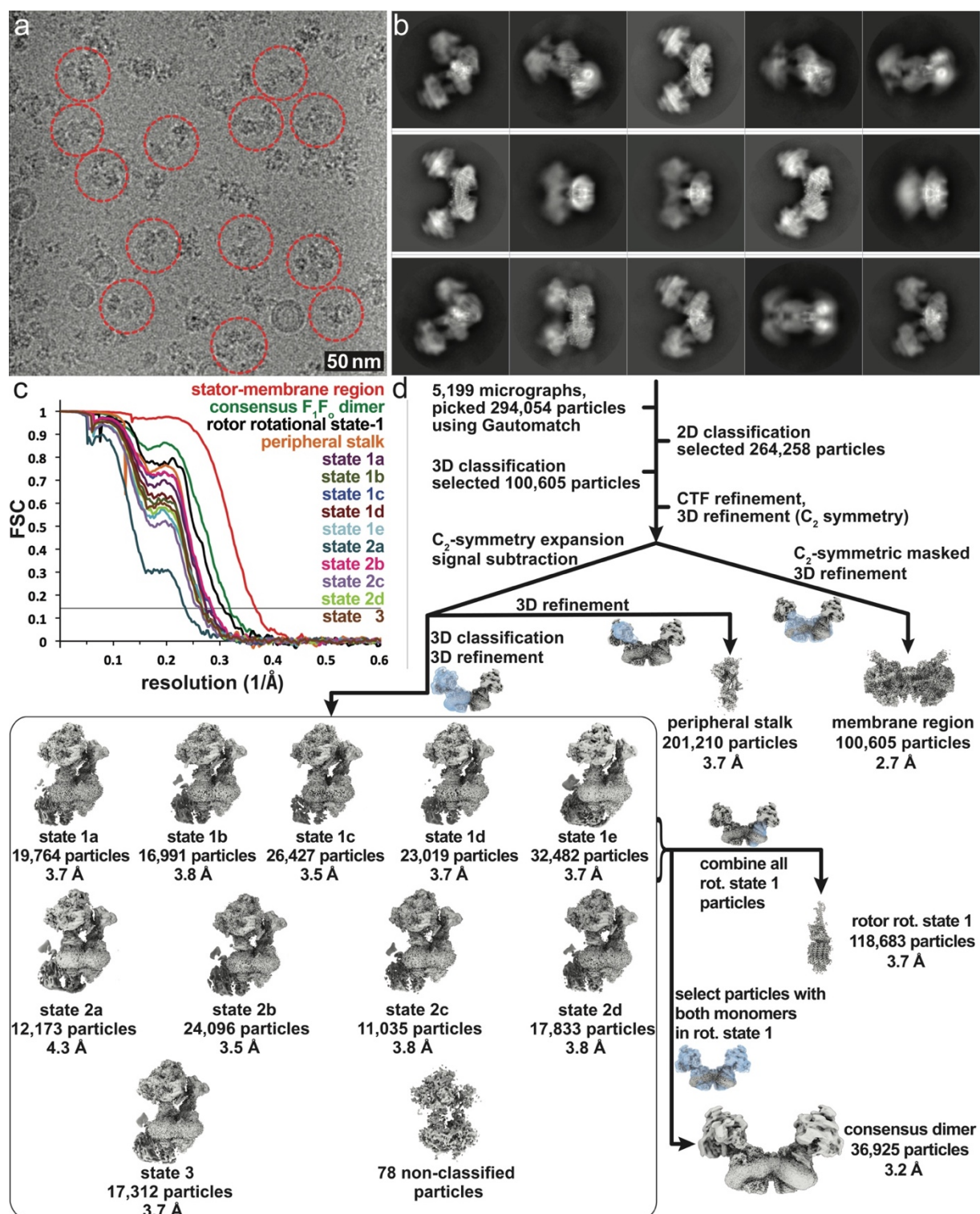
Supplementary figure 2: Cryo-EM data processing of the *T. brucei* ATP synthase dimer. **a**, Representative micrograph. **b**, 2D class averages. **c**, Fourier Shell Correlation (FSC) curves showing the estimated resolutions of ATP synthase maps according to the gold standard 0.143 criterion. **d**, Data processing scheme resulting in maps covering all regions of the complex, as well as 10 rotational states.

30

811
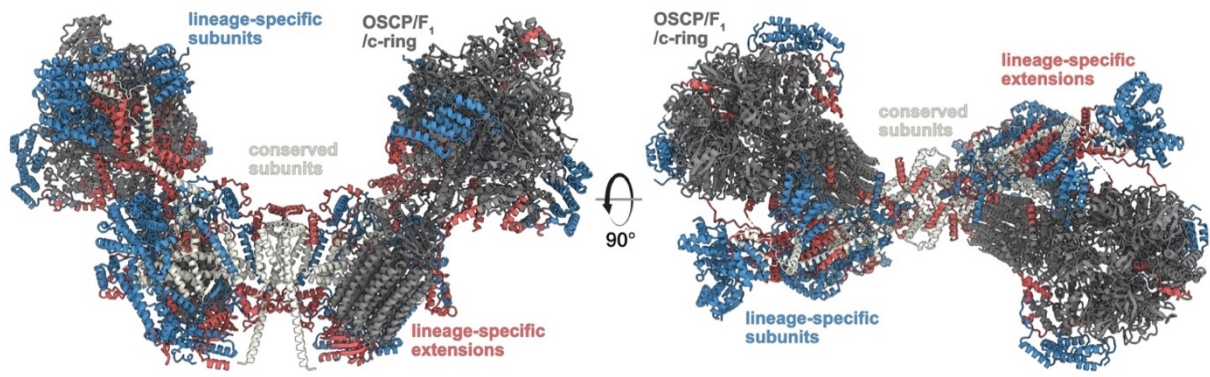
Supplementary figure 3: Conserved and phylum specific elements generate the *T. brucei* ATP synthase architecture. The canonical OSCP/F_1/c-ring monomers (dark grey) are tied together by both conserved F_o subunits and extensions of lineage-specific subunits (red). The F_o periphery and peripheral stalk attachment are composed of lineage specific subunits (blue).

31
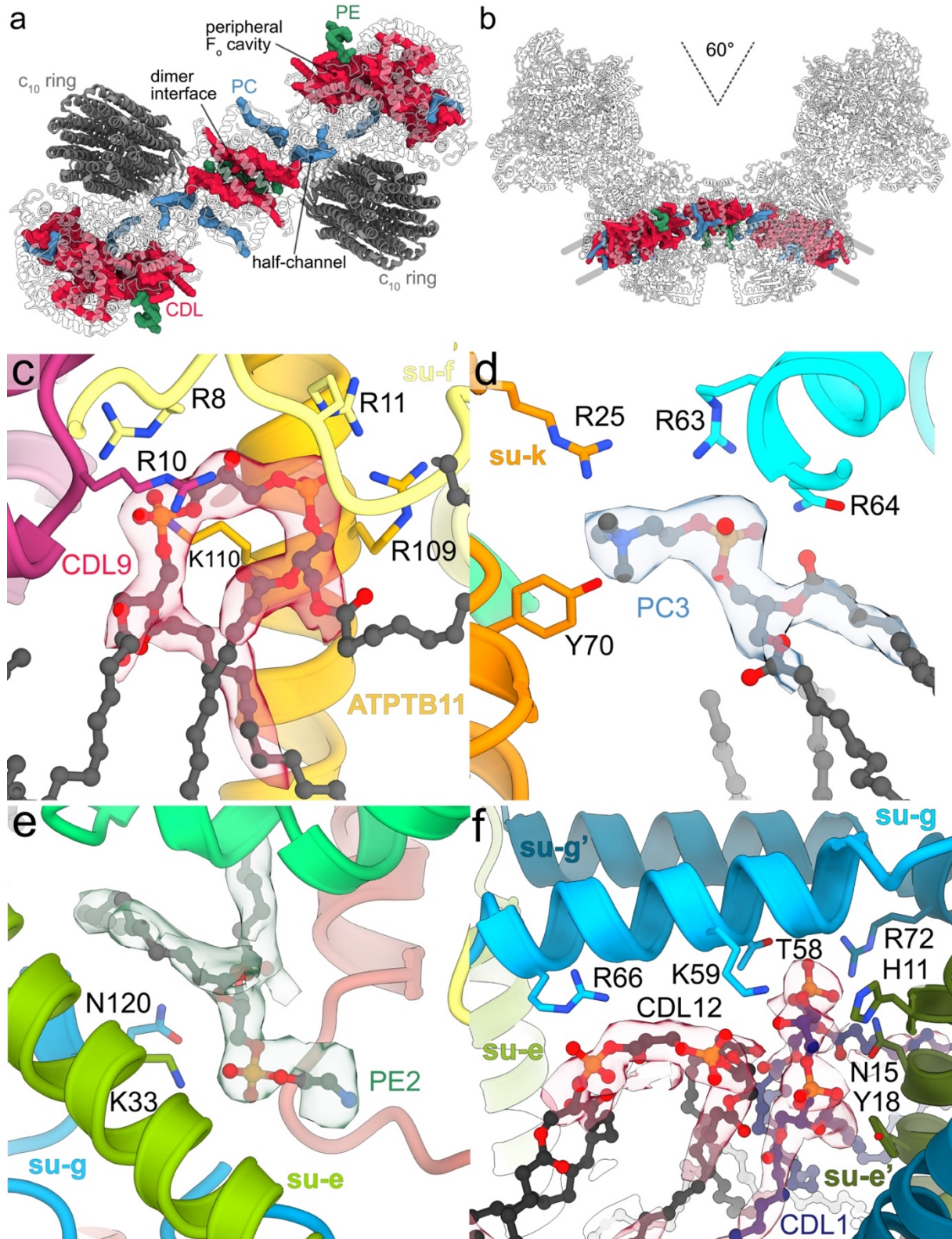
Supplementary figure 4: The F_o region coordinates numerous bound lipids. a, F_o top view, cardiolipin (CDL), phosphatidylcholine (PC) and phosphatidlyethanolamine (PE) are bound at the dimer interface, the lumenal proton half-channel and the peripheral F_o cavity. **b**, The 60°-dimer angle generates a curved F_o region with phospholipids bound in an arc-shaped bilayer. **c-f**, Bound lipids with cryo-EM density and coordinating residues.
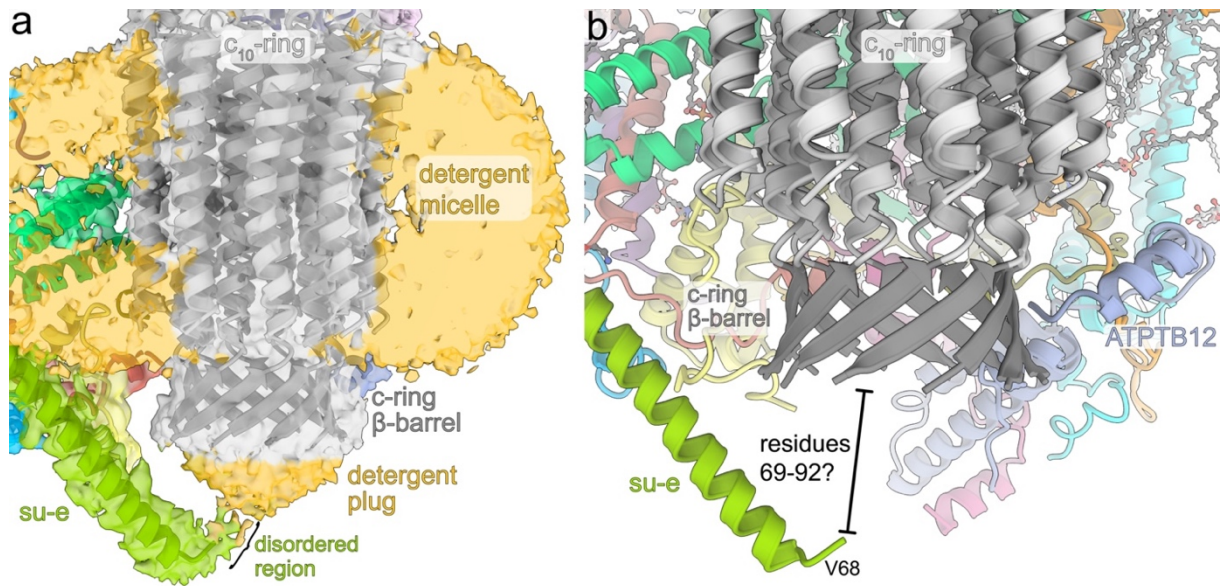
823

824
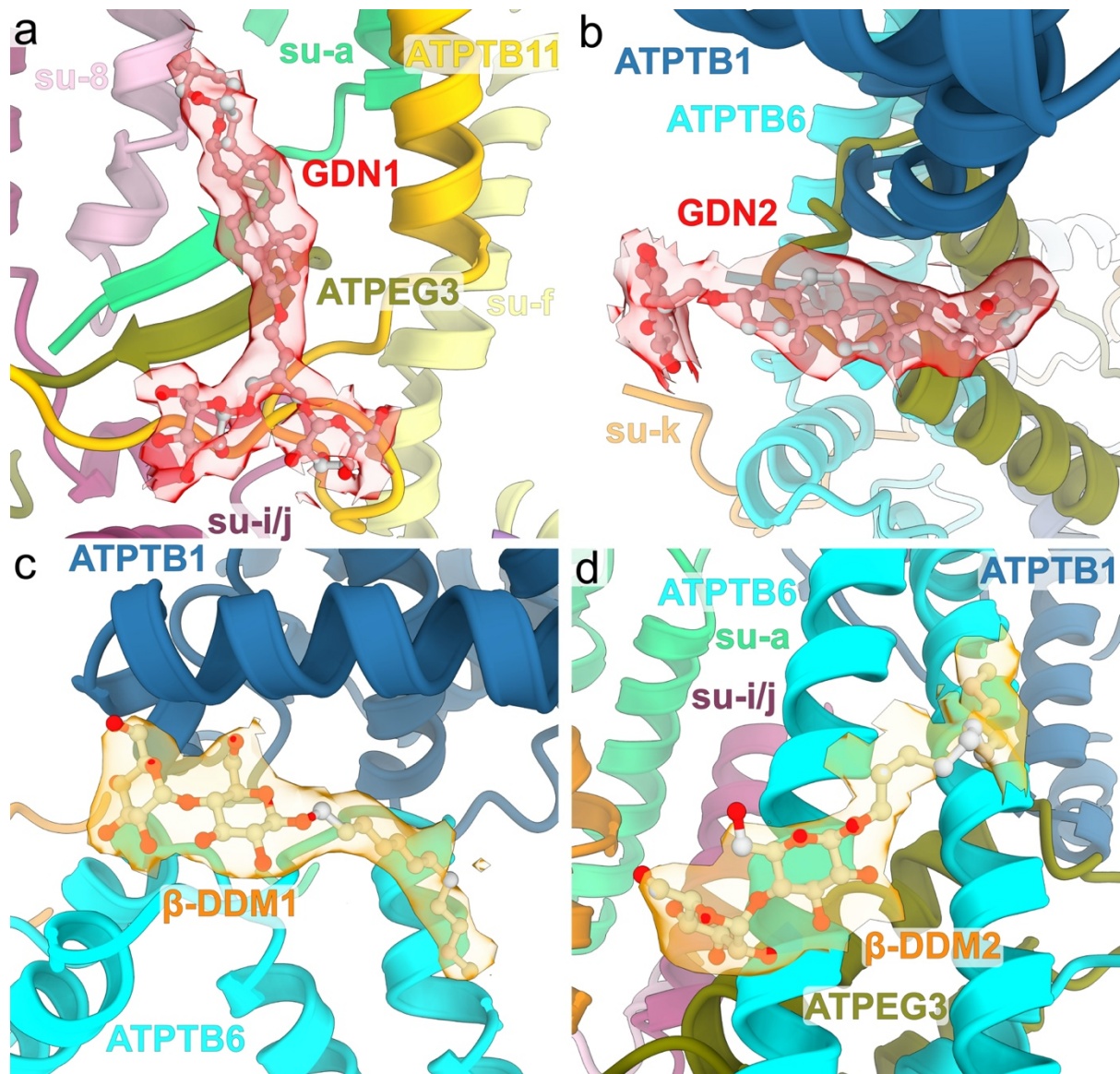
Supplementary figure 5: Bound detergents of the F_o region. GDN **(a,b)** and β-DDM **(c,d)** molecules bound in the periphery of the membrane region with cryo-EM map densities shown (transparent), indicating that both glycosides are retained in the detergent micelle.

828

33

829

830 **Supplementary figure 6. The C-terminal tail of subunit-*e* interacts with the c_{10}-ring. a,**
831 The cryo-EM map reveals disordered detergent density of the detergent belt surrounding the
832 membrane region as well as a detergent plug on the luminal side of the *c*-ring. **b,** The helical
833 C-terminus of subunit-*e* extends into the lumen towards the *c*-ring. The terminal 23 residues
834 are disordered and likely interact with the β-barrel.
835

34

836

35
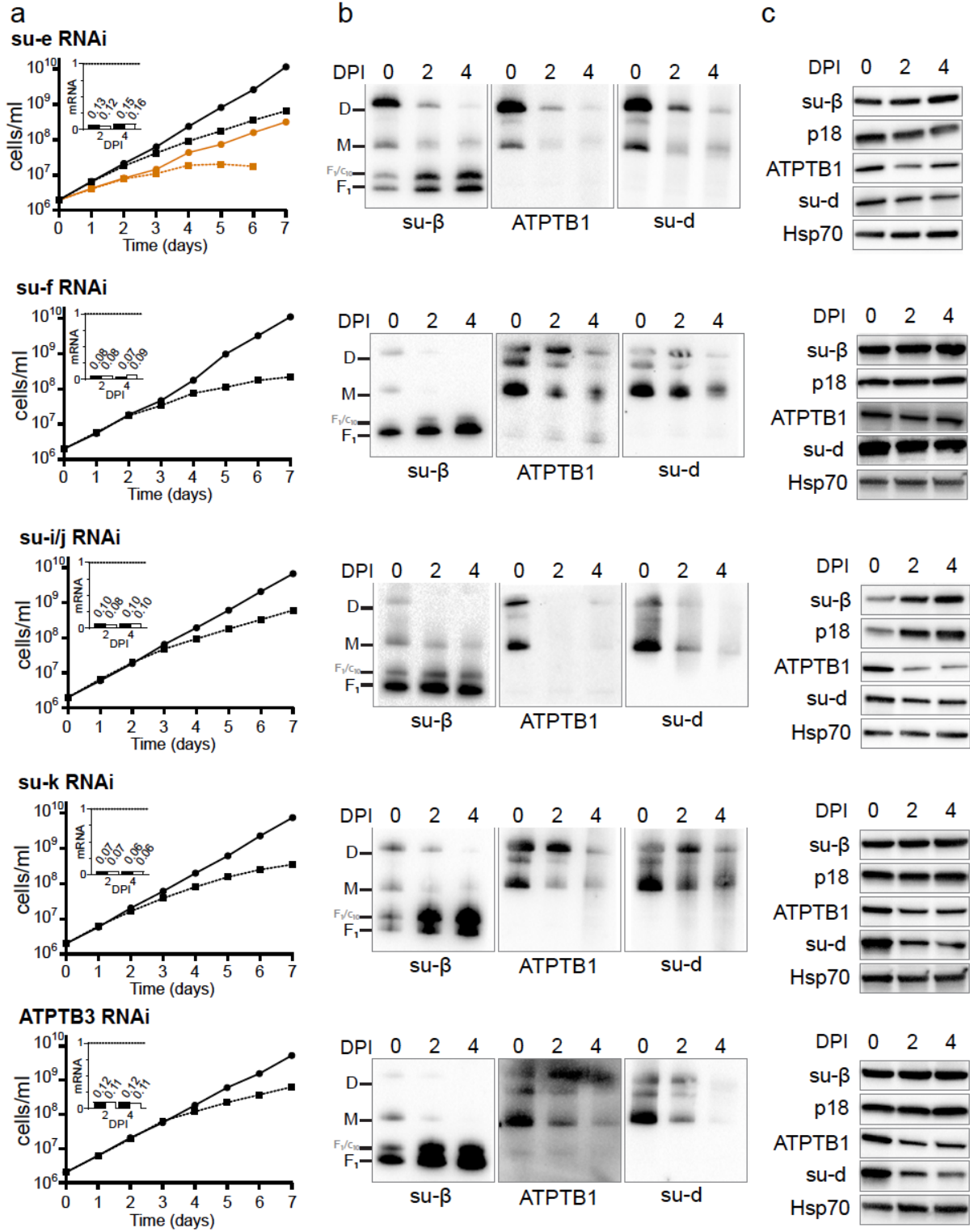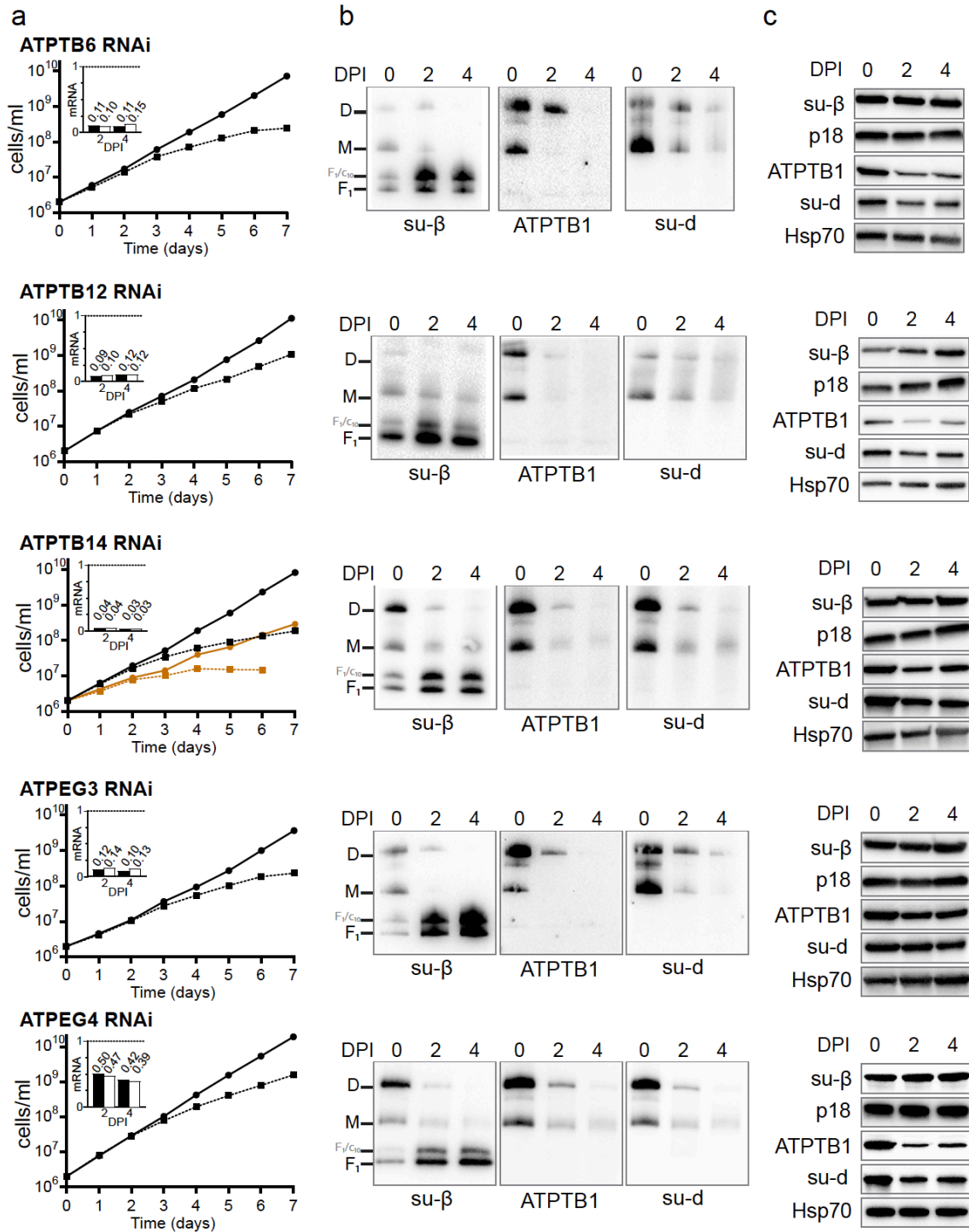
Supplementary figure 7. Effects of RNAi knock-down of ATP synthase subunits on viability and stability and dimerization of ATP synthase. a, Growth curves of indicated non-induced (solid lines) and tetracycline induced (dashed lines) RNAi cells lines in the presence (black) or absence (brown) of glucose. The insets show relative levels of the respective target mRNA at indicated days post induction (DPI) normalized to the levels of 18S rRNA (black bars) or ß-tubulin (white bars). **b**, Immunoblots of mitochondrial lysates from indicated RNAi cell lines resolved by BN-PAGE probed by antibodies against indicated ATP synthase subunits. **c**, Immunoblots of whole cell lysates from indicated RNAi cell lines probed with indicated antibodies.

36

847

848
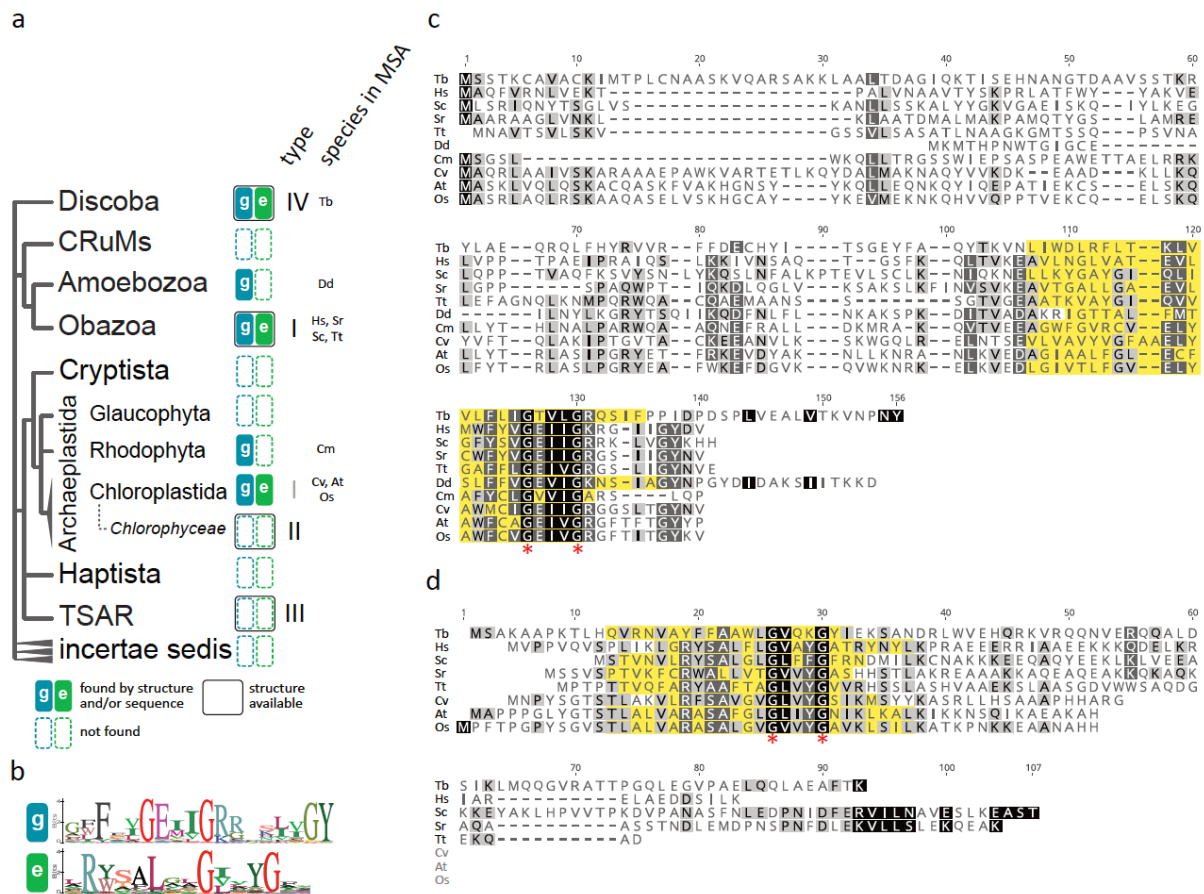
Supplementary figure 8: Phylogenetic distribution and sequence conservancy of subunits *e* and *g*. a, Distribution of subunits *e* and *g* mapped on the phylogenetic tree of eukaryotes[3]. Homologs of subunits *e* and *g* were searched in non-redundant GenBank and UniprotKB protein databases by PSI-BLAST, and phmmer and hmmsearch[4], respectively, using individual sequences of representatives from *H. sapiens* and *T. brucei*, and in the case of hmmsearch a multiple sequence alignment (MSA) of representatives from *Homo sapiens*, *Saccharomyces cerevisiae*, *Arabidopsis thaliana* and *T. brucei*, as queries. Groups, in which at least one structure of ATP synthase is available, are marked. Abbreviations of species used in MSA in panels (c) and (d) are shown. **b**, Sequence logo of GXXXG motifs and flanking regions of subunits *e* and *g*. Hits from hmmsearch were clustered by CD-HIT Suite[5] to 50% sequence identity and MSA of representative sequences of each cluster was generated by Clustal Omega4[6]. The sequence logos were created from MSA in Geneious Prime (Biomatters Ltd.). **c,d**, MSA of sequences of subunits g (c) and e (d) from species representing major groups shown in (a) generated by MUSCLE[7] and visualized in Geneious Prime. The experimentally determined or predicted transmembrane regions are highlighted in yellow. Species abbreviations: Tb – *T. brucei*, Hs – *H. sapiens*, Sc – *S. cerevisiae*, Sr – *Salpingoeca rosetta*, Tt – *Thecamonas trahens*, Dd – *Dictyostelium discoideum*, Cm – *Cyanidioschyzon merolae*, Cv – *Chlorella vulgaris*, At – *Arabidopsis thaliana*, Os – *Oryza sativa*.

867

868

Supplementary references:

1. Subrtova, K., Panicucci, B. & Zikova, A. ATPaseTb2, a unique membrane-bound FoF1-ATPase component, is essential in bloodstream and dyskinetoplastic trypanosomes. *PLoS Pathog* **11**, e1004660 (2015).

2. Panigrahi, A.K. et al. Mitochondrial complexes in Trypanosoma brucei: a novel complex and a unique oxidoreductase complex. *Mol Cell Proteomics* **7**, 534-45 (2008).

3. Burki, F., Roger, A.J., Brown, M.W. & Simpson, A.G.B. The New Tree of Eukaryotes. *Trends Ecol Evol* **35**, 43-55 (2020).

4. Protein Sequence Similarity Search. *Curr Protoc Bioinformatics* **60**, 3 15 1-3 15 23 (2017).

5. Huang, Y., Niu, B., Gao, Y., Fu, L. & Li, W. CD-HIT Suite: a web server for clustering and comparing biological sequences. *Bioinformatics* **26**, 680-2 (2010).

6. Sievers, F. et al. Fast, scalable generation of high-quality protein multiple sequence alignments using Clustal Omega. *Mol Syst Biol* **7**, 539 (2011).

7. Edgar, R.C. MUSCLE: multiple sequence alignment with high accuracy and high throughput. *Nucleic Acids Res* **32**, 1792-7 (2004).